ABSTRACT

Title of Dissertation: STATISTICS OF IMPEDANCE AND SCATTERING

MATRICES IN CHAOTIC MICROWAVE CAVITIES:

THE RANDOM COUPLING MODEL

Xing Zheng, Doctor of Philosophy, 2005

Dissertation directed by: Professor Edward Ott
Professor Thomas M. Antonsen, Jr.
Department of Physics

A model is proposed for the study of the statistical properties of the impedance
(Z) and scattering (S) matrices of open electromagnetic cavities with several
transmission lines or waveguides connected to the cavity. The model is based on
assumed properties of the eigenfunctions for the closed cavity. Analysis of the
model successfully reproduces features of the random matrix model believed to
be universal, while at the same time incorporating features which are specific to
individual systems. Universal statistical properties of the cavity impedance Z
are obtained in terms of the radiation impedance. These universal properties are
independent of system-specific details and shared by the members of the general
class of systems whose corresponding ray trajectories are chaotic.

In the single channel case, I obtained the normalized impedance and scattering coefficients whose probability density functions (PDF) are predicted to be universal. In the multiple-channel case, I focused on correlations in the phases of the eigenvalues of the S-matrix, and derived a formula for the averaged reflection coefficients in terms of the port radiation impedance. Effects of time-reversal symmetry and wall absorption are discussed. Furthermore, I study the characterization of statistical fluctuations of the scattering matrix S and the impedance matrix Z, through their variance ratios. The variance ratio for the impedance matrix is shown to be a universal function of distributed losses within the scatterer, which contrasts with variance ratio of the scattering matrix for which universality applies only in the large loss limit. Theoretical predictions are tested by direct comparison with numerical solutions for a specific system, and also agree with experimental results obtained from scattering measurements on a chaotic microwave cavity.

STATISTICS OF IMPEDANCE AND SCATTERING

MATRICES IN CHAOTIC MICROWAVE CAVITIES:

THE RANDOM COUPLING MODEL

by

Xing Zheng

Dissertation submitted to the Faculty of the Graduate School of the
University of Maryland, College Park in partial fulfillment
of the requirements for the degree of
Doctor of Philosophy
2005

Advisory Committee:

      Professor Edward Ott, Chairman/Advisor
      Professor Thomas M. Antonsen, Jr.
      Professor Victor L. Granatstein
      Professor Steven M. Anlage
      Associate Professor Brian R. Hunt

DEDICATION

To my family:

Lin, Robert and Jackey

ACKNOWLEDGMENTS

TABLE OF CONTENTS

LIST OF FIGURES

Chapter 1

Introduction

1.1 Overview of Statistical Electromagnetics

The problem of the coupling of electromagnetic radiation in and out of structures is a general one which finds applications in a variety of scientific and engineering contexts. Examples include the susceptibility of circuits to electromagnetic interference, the confinement of radiation to enclosures, and the coupling of radiation to accelerating structures in particle accelerators [1–3].

Because of the wave nature of radiation, the coupling properties of a structure depend in detail on the size and shape of the structure, as well as the frequency of the radiation. In considerations of irregularly shaped electromagnetic enclosures for which the wavelength is fairly small compared with the size of the enclosure, it is typical that the electromagnetic field pattern within the enclosure, as well as the response to external inputs, can be very sensitive to small changes in frequency and to small changes in the configuration. Thus, knowledge of the response of one configuration of the enclosure may not be useful in predicting that of a nearly identical enclosure. This motivates a statistical approach to the electromagnetic problem. A good introduction and overview is provided in the

book by Holland and St. John [4].

While our ability to numerically compute the response of particular structures has advanced greatly in recent years, the kind of information needed for a statistical description may not be obtainable directly from numerical computation. In the case of complex or irregularly shaped enclosures that are large compared to a wavelength, accurate numerical solution of the electromagnetic field problem can be difficult or impossible. Also, if such numerical solutions are to be used to generate statistics, the numerical solutions must be obtained for many slightly different configurations and/or frequencies.

Thus it would seem to be desirable to have specific analytical predictions for the statistics of electromagnetic quantities in such circumstances. This general problem has received much attention in previous work (e.g., Refs. [5–7]). Some of the main issues addressed in these works are: the probability distribution of fields at a point, the correlation function of fields at two points near each other, the statistics of the excitation of currents in cables or in small devices within the enclosure, the cavity Q, the statistics of coupling to the enclosure, and the statistics of scattering properties. A fundamental basis for most of these studies is that, due to the complexity of the enclosure and the smallness of the wavelength compared to the enclosure size, the electromagnetic fields approximately obey a statistical condition that we shall call *the random plane wave hypothesis*, which we will explain more carefully in the next section.

1.2   Wave Chaos Approach

In addition to this previous work on *statistical electromagnetics*, much related work has been done by theoretical physicists. The physicists are interested in

solutions of quantum mechanical wave equations when the quantum mechanical wavelength is short compared with the size of the object considered. Even though the concern is not electromagnetics, the questions addressed and the results are directly applicable to wave equations, in general, and to electromagnetics, in particular. The start of this line of inquiry was a paper by Eugene Wigner [8]. Wigner's interest was in the energy levels of large nuclei. Since the energy level density at high energy is rather dense, and since the solution of the wave equations for the levels was inaccessible, Wigner proposed to ask statistical questions about the levels. Wigner's results apply directly to the statistics of resonant frequencies in highly-overmoded irregularly-shaped electromagnetic cavities. Since Wigner's work, and especially in recent years, the statistical approach to wave equations has been a very active area in theoretical physics, where the field has been called 'quantum chaos' [9, 10]. Much work has been done elucidating the consequences for the scattering of waves in cases in which, in the geometric optics approximation, the ray orbits within the structure are chaotic. Examples include optical [11], acoustic [12], microwave [13–16] and electronic cavities [17, 18]. We emphasize, however, that the quantum aspect to this work is not inherent, and that a better terminology, emphasizing the generality of the issues addressed, might be 'wave chaos'. In Sec. 1.2 I will review previous work that is relevant to the subsequent discussion in the dissertation. Most of this review concerns work done in the context of quantum mechanics and can also be found in Refs. [19–21].

1.2.1 Eigenvalue Statistics

In considering a closed system Weyl [23] gave a result for the approximate average eigenvalue density in the limit of small wavelength compared to the system size. For the two-dimensional problem $(\nabla^2 + k^2)\phi = 0$ in a region R of area A with Dirichlet or Neumann boundary conditions on ϕ, Weyl's formula reduces to

$$\tilde{\rho}(k^2) \cong A/4\pi , \tag{1.1}$$

where $\tilde{\rho}(k^2)\delta k^2$ is the number of eigenvalues k_n^2 ($k_1^2 \leq k_2^2 \leq k_3^2 \leq \ldots$) between $(k^2 - \delta k^2/2)$ and $(k^2 + \delta k^2/2)$. The quantity $\Delta(k^2) = 1/\tilde{\rho}(k^2)$ is the average spacing between eigenvalues, i.e., average of $(k_{n+1}^2 - k_n^2)$ for $k_n^2 \cong k^2$. Inherent in the derivation of (1.1) are the assumptions that $\delta k^2 \ll k^2$ and that many modes are present in the range δk^2. These imply the requirement that $k^2 A \gg 4\pi$, the previously mentioned small wavelength limit. Higher order corrections to the Weyl formula (e.g., terms of order ℓ/k added to the right hand side of (1.1), where ℓ is a relevant length of the boundary) have been given in Refs. [24, 25]. Other corrections due to Gutzwiller are oscillatory in k and are geometry dependent [20, 26]. For a three dimensional electromagnetic enclosure Weyl's formula becomes $\Delta(k^2) = 1/\tilde{\rho}(k^2) = 2\pi^2/kV$, where V is the volume of the enclosure. We note that $\Delta(k^2)$ depends on k in the three dimensional case, but is k-independent in two dimensions. Since we work primarily in two dimensions, we henceforth use the notation Δ in place of $\Delta(k^2)$.

If one examines the spacings between two adjacent eigenvalues, $k_{n+1}^2 - k_n^2$, then, *on average* it is well-approximated by $1/\Delta$ with Δ given by the Weyl formula. However, the fluctuations from the average are themselves typically of order $1/\Delta$. Thus it is of interest to consider the distribution function of the eigenvalue spacings for a random choice of adjacent eigenvalues in the range $(k^2 - \delta k^2/2)$

to $(k^2 + \delta k^2/2)$. As a first step we can normalize the spacings using the Weyl formula,

$$s_n = (k_{n+1}^2 - k_n^2)/\Delta . \qquad (1.2)$$

Wigner considered the probability distribution function for the eigenvalues (energy levels) of large complicated nuclei. Depending on symmetries, he found three cases, only two of which are relevant for us. These two cases are referred to as the Gaussian Orthogonal Ensemble (GOE) and the Gaussian Unitary Ensemble (GUE) (to be explained subsequently). Wigner's results for the probability distributions $P(s)$ of the normalized spacing (1.2) are [8, 19]

$$P_{GOE}(s) \cong (\pi/2)s \exp(-\pi s^2/4) , \qquad (1.3)$$

and

$$P_{GUE}(s) \cong (32/\pi)s^2 \exp(-4s^2/\pi) . \qquad (1.4)$$

These spacing distributions, while derived for a very specific model, have been found to apply in a variety of contexts, including the spacing distributions for modes of electromagnetic resonators, as demonstrated experimentally in Ref. [27].

1.2.2   Random Matrix Theory

We now explain the idea behind Wigner's derivations of (1.3) and (1.4), first considering (1.3) which applies to our example, the eigenvalue problem,

$$(\nabla^2 + k^2)\phi = 0 \quad \text{in} \quad R , \qquad (1.5)$$

$$\phi = 0 \quad \text{on the boundary of } R , \qquad (1.6)$$

where R is a finite connected two dimensional domain and $\nabla^2 = \partial^2/\partial x^2 + \partial^2/\partial y^2$. Introducing a real orthogonal basis $\psi_j(x, y)$ $(j = 1, 2, \ldots)$, where ψ_j satisfies

the boundary condition (1.6) [note, ψ_j are in general *not* the solutions of the eigenvalue problem (1.5,1.6)], we express $\phi(x,y)$ as $\phi(x,y) = \sum_j c_j \psi_j$, and insert this expansion in (1.5). Multiplying by ψ_i and integrating over R we obtain the infinite matrix problem,

$$Hc = \Lambda c \ , \tag{1.7}$$

where $\Lambda = -k^2$, $c = (c_1, c_2, \ldots)^T$ (the superscribed T denotes the transpose), and the elements of H are

$$H_{ij} = \int \int_R \psi_i \nabla^2 \psi_j dx dy \ . \tag{1.8}$$

Note that, aside from the conditions of orthogonality and the satisfaction of the boundary conditions, Eq. (1.6), the basis functions $\psi_j(x,y)$ are so far arbitrary. Nevertheless, we still know something about the matrix H: It is real, and, via integration of (1.8) by parts, it is also symmetric. Wigner hypothesized that the eigenvalue spectrum of complicated nuclear systems have similar statistical properties to those of the spectra of ensembles of random matrices. Wigner further hypothesized that the following two statistical conditions on the probability distribution $\bar{P}(H)$ for the ensemble of matrices should be satisfied.

(1) *Invariance.* The probability distribution should be independent of the choice of basis $\{\psi_i\}$. Expressing the eigenvalue problem (1.7) in another orthogonal basis $\{\psi_i'\}$, invariance requires

$$\bar{P}(H) = \bar{P}(OHO^T), \tag{1.9}$$

for all orthogonal matrices O.

(2) *Independence.* The matrix elements (aside from the symmetry $H_{ij} = H_{ji}$) are independent random variables. Thus $\bar{P}(H)$ is the product of distributions for all the individual elements H_{ij}, $i \leq j$.

These two conditions can be shown to imply [8, 9, 19] that the distributions for the H_{ij} are all Gaussians, that the variances of the off diagonal elements are all the same, and that the variances of all the diagonal element distributions are double the variance of the off diagonal elements. This specifies the Gaussian Orthogonal Ensemble (GOE) of random matrices. Using this distribution for H, Wigner derived Eq. (1.3) for the normalized spacing distribution.

Wigner's second result (1.4) applies to situations in which 'time reversal symmetry is broken'. To simply see the origin of this terminology, consider the motion of a point charge in a homogeneous magnetic field $B_0\hat{z}_0$. The motion in the (x, y) plane is circular. If, at any time $t = t_0$, we stop the charge, and reverse its velocity, it does not retrace its path, but, as illustrated in Fig. 1.1(a), it follows a different circular path. In contrast, the motion of a particle in an arbitrary potential does retrace its path upon reversal of its velocity vector, if there is no magnetic field. The impact of this is that the quantum mechanical wave equation becomes complex; that is, unlike (1.5) and (1.6), there are imaginary terms present, and these typically cannot be removed by a change of variables. Thus, expanding as before, H is now a complex Hermitian matrix, $H_{ij} = H_{ji}^*$, and (1.9) is replaced by

$$\bar{P}(H) = \bar{P}(UHU^\dagger) \,, \tag{1.10}$$

where U is an arbitrary unitary matrix, $U^{-1} = U^\dagger$, with $\dagger$ standing for the conjugate transpose of the matrix. Application of (1.10) and the independence hypothesis, then leads to the Gaussian Unitary Ensemble (GUE) of random matrices. The statistics for the normalized eigenvalue spacings in the GUE case is given by (1.4).

The GUE statistics are also relevant to electromagnetics [27]. In particular, if
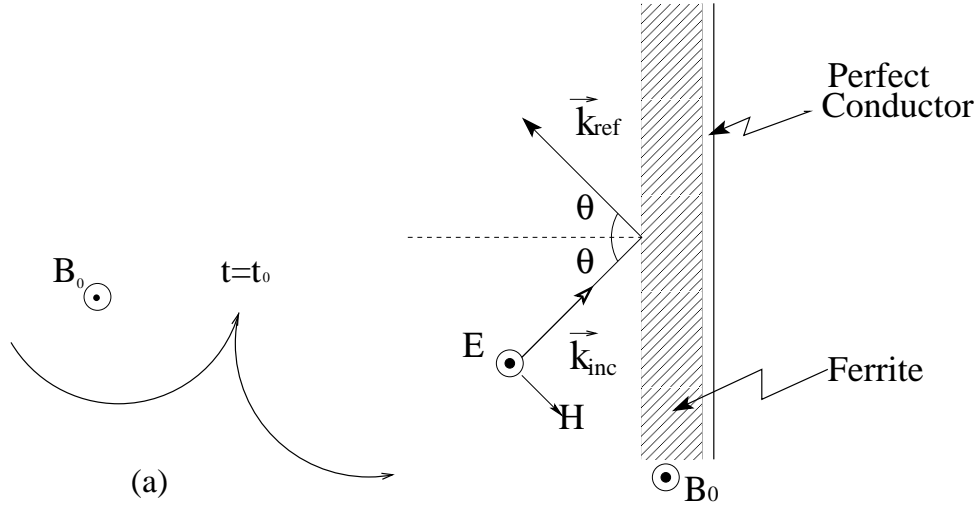
Figure 1.1: Time reversal symmetry breaking (a) for a particle trajectory in a magnetic field, and (b) for reflection from a lossless magnetized ferrite slab.

a lossless magnetized ferrite is present, the basic wave equation becomes complex because the magnetic permittivity matrix μ is Hermitian, $\mu = \mu^{\dagger}$, with complex off-diagonal elements. As an example of the breaking of 'time reversal symmetry' in the case of a magnetized ferrite, consider Fig. 1.1(b) which shows a homogeneous lossless ferrite slab, with vacuum in the region to its left, a perfectly conducting surface bounding it on its right, a constant applied magnetic field $B_0\hat{z}_0$, and a time harmonic electromagnetic plane wave incident on the slab from the left where the angle of incidence is θ. The resulting reflection coefficient for the situation in Fig. 1.1(b) has magnitude one due to energy conservation, and is thus given by the phase shift $\alpha(\theta, B_0)$ upon reflection. If we now reverse the arrows in Fig. 1.1(b), the phase shift is different from what it previously was if $B_0 \neq 0$, but is the same if $B_0 = 0$. Thus here too a magnetic field may be said to break time reversal symmetry.

The study of random ensembles of matrices, particularly the GOE and GUE ensembles initiated by the work of Wigner, has become a very highly developed field [22, 28]. Using these ensembles many questions, other than that of finding $P(s)$, have been addressed. We will come back to this later in the dissertation.

1.2.3 Chaotic Ray Trajectories

Wigner's original setting was a very complicated wave system, and it was this complication that he invoked to justify the validity of a statistical hypothesis. Subsequently it was proposed [29, 30] that, under appropriate conditions, even apparently simple systems might satisfy the Wigner hypotheses. The idea was that, since the wavelength is short, the ray equations should indicate the character of solutions of the wave equation. Considering the example of a vacuum-filled two dimensional cavity (i.e., it is thin in z), the ray equations are the same as those for the trajectory of a point particle: straight lines with specular reflection (i.e., angle of incidence equals angle of reflection) at the boundaries. Such systems are called 'billiards' and have been studied since the time of Birkhoff [31] as a paradigm of particle motion in Hamiltonian mechanics. It is found that typically three different types of motion are possible: (a) integrable, (b) chaotic, and (c) mixed. Whether (a), (b) or (c) applies depends on the shape of the boundary; e.g., see Fig. 1.2. It is noteworthy that even rather simple boundaries can give chaotic behavior. Thinking of chaotic behavior as complicated, the authors of Refs. [29, 30] proposed that Wigner's hypotheses might apply in situations where the system was simple but the dynamics was chaotic (complicated), and they tested this proposal numerically, obtaining results in good agreement with the predicted $P_{GOE}(s)$, Eq. (1.3). In addition, subsequent experimental [27, 32, 33] work in

electromagnetic cavities, both with and without magnetized ferrite, support the applicability of Wigner's hypotheses to simple ray-chaotic systems.

Figure 1.2 gives some examples of billiard (or cavity) shapes. The rectangle of Fig. 1.2(a) is an example of an integrable system; particle orbits *separately* conserve the kinetic energies associated with their motion in the x-direction and in the y-direction. On the other hand, this is not true for the examples of chaotic billiard (cavity) shapes shown in Figs. 1.2(b-e). For these chaotic shapes, the following situation applies. Suppose we pick an initial condition for the particle orbit at random by first choosing a point within the billiard with uniform probability density per unit area and by next choosing an angle θ with uniform probability in 0 to 2π. We then launch the particle with speed v from the chosen point and in a direction θ to the horizontal. With probability one, the resulting orbit will fill the cavity uniformly and isotropically.

Thus one qualitative difference between the billiard orbits from randomly chosen initial conditions for an integrable case, like Fig. 1.2(a), as opposed to chaotic cases, like Figs. 1.2(b-e), is that the velocity direction samples all orientations equally at all spatial points in the chaotic case, but not in the integrable case. Another, perhaps more fundamental, difference is that, if we start two initial conditions at the same (or slightly different) location and with the same speed, but with slightly different angular orientations of their velocity vectors, then the character of the subsequent evolutions of the two orbits is different in the integrable and chaotic cases. In both cases, the two orbits typically separate from each other, but in the integrable case the separation is, on average, proportional to time, while in the chaotic case it is, on average, exponential with time.
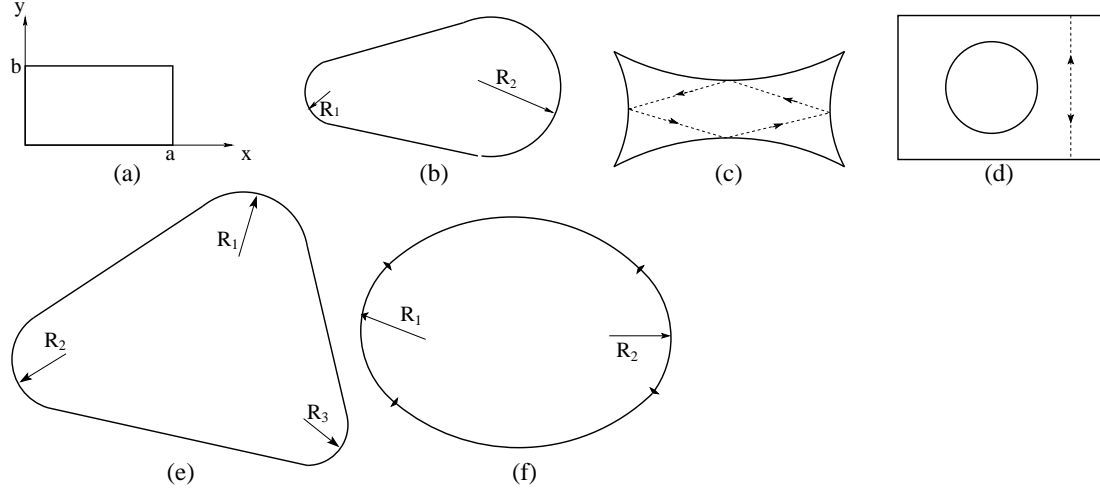
Figure 1.2: Examples of billiard shapes. (a) Is a rectangle. (b) Is made up of two circular arcs of radii R_1 and R_2 that are tangent at the point of joining to two straight line segments. The sides of (c) are circular arcs. The billiard region of (d) lies between the circle and the square. (e) Is similar to (b). (d) Is made up of four circular arcs that join smoothly at the dots indicated on the boundary; the centers of the upper and lower arcs lie outside the billiard region while the other two arcs of radii R_1 and R_2 have centers that are within the billiard region. (a) Is integrable, (b)-(e) are chaotic, and (f) is mixed.

1.2.4 The Random Plane Wave Hypothesis

As mentioned in the first section, the basis for much of the previous work on statistical electromagnetics is 'the random plane wave hypothesis' that, in a suitable approximate sense, the fields within the cavity behavior like a random superposition of isotropically propagating plane waves. The same hypothesis has also been used for waves in plasmas [34] and within the context of quantum mechanics of classically chaotic systems [35]. A strong motivation for this hypothesis is the observation that ray orbits in chaotic systems (like the billiards in Figs. 1.2(b-e)) are uniform in space and isotropic in direction. Furthermore, direct numerical tests in two dimensional chaotic cavities tend to support the hypothesis [29].

We also note that different predictions result from the random plane wave hypothesis in the cases of time reversal symmetry (i.e., real waves) and of broken time reversal symmetry (i.e., complex waves), and these have been tested in microwave cavity experiments with and without magnetized ferrites [36]. We discuss the case of broken time reversal symmetry further in chapter 4.

In our subsequent work in this dissertation, we mainly employ the random plane wave hypothesis, although use will occasionally also be made of random matrix theory (in particular, we will use Eqs. (1.3) and (1.4)). As will become evident, the random matrix hypotheses of Wigner are closely related to the random plane wave hypothesis. Because the random plane wave hypothesis has a somewhat closer connection to the physical aspects of the problem, it allows a more transparent means of taking into account the nonuniversal effects of the port geometry.

While the random plane wave hypothesis is mostly confirmed by numerical tests, it is also observed that it is sometimes violated. In particular, when many

eigenmodes of a very highly overmoded, two-dimensional cavity are computed and examined, it is found, for most modes, that the energy density is fairly uniformly distributed in space over length scales larger than a wavelength [29, 37]. This is in accord with the random plane wave hypothesis. On the other hand, it is also found [37–40] that there is some small fraction of modes for which energy density is observed to be abnormally large along unstable periodic orbits. For example, for a cavity shaped as in Fig. 1.2(c), a short wavelength mode has been found [40] for which there is enhanced energy density in the vicinity of the dashed, diamond-shaped orbit shown in Fig. 1.2(c). This phenomenon has been called 'scarring' [37]. One conjecture is that, as the wavelength becomes smaller compared to the cavity size, scarring becomes less and less significant, occurring on a smaller and smaller fraction of modes and with smaller energy density enhancement near the associated periodic orbit [40]. In our work to follow, we will neglect the possibility of scarring. We also note that the scar phenomenon is not included in the random matrix theory approach.

1.3   Outline of Dissertation

In this dissertation I consider an irregularly shaped cavity with transmission lines and/or waveguides connected to it, and I attempt to obtain the statistical properties of the impedance matrix Z and the scattering matrix S. I will mainly treat the case of cavities that are thin in the vertical (z-direction) direction, so that the problem admits a purely scalar formulation. While the two dimensional problem has practical interest in appropriate situations (e.g., the high frequency behavior of the power plane of a printed circuit), we emphasize that our results for the statistical properties of Z and S matrices are predicted to apply equally well

to three dimensional electromagnetics and polarized waves. Due to the analogy between Helmholtz equation and Schödinger equation, we expect our models can be applied to quantum systems.

This dissertation is organized as follows:

- In Chapter 2, I derive expressions for the impedance and scattering matrices in terms of eigenvalues and eigenfunctions, in the context of a microwave cavity with ports connected to it. This approach is closely related to Wigner's R-theory. A novel part of our model is that it expresses the cavity impedance in terms of the radiation impedance, which characterizes the system dependent details of the coupling.

- In Chapter 3, I use our model to investigate the impedance statistics in the simplest case, i.e., a lossless time reversal symmetric cavity connected to a single port. We construct a model normalized impedance to compare with the theoretical prediction, and test our results by comparison with data obtained from numerical solutions of the Helmholtz wave equations for a chaotic cavity shape.

- In Chapter 4, I discuss several aspects of model generalization. First, we extend our discussion from single port to multiport; second, effects of time reversal symmetry breaking are described. Also discussed is an investigation of loss effects on the impedance matrix, particularly, the marginal distributions of the real and imaginary parts of the impedance, and their correlations at different frequencies.

- In Chapter 5, I describe the statistics of scattering coefficient (one port case) and scattering matrix (multiple ports). In the one-port case, I fo-

cus on the probability density function of phase distribution, which, after normalization, is uniformly distributed. In the case of multiple ports, formulae regarding the averaged transmission coefficients versus the coupling are presented.

- In Chapter 6, a characterization of fluctuations of impedance and scattering matrices is given in terms suitably defined the impedance and scattering variance ratios. It is found that the variance ratio for the impedance is a universal function of distributed losses within the scatterer.

- In Chapter 7, I give a summary of our work and discuss possible future work.

Chapter 2

Random Coupling Model

2.1 Formulation for Z and S Matrix

For an electrical circuit or electromagnetic cavity with ports, the scattering matrix is related to the impedance matrix Z. The impedance matrix provides a characterization of the structure in terms of the linear relation between the voltages and currents at all ports (for a cavity with a waveguide port, the concepts of voltages and currents can be appropriately generalized to describe the waveguide modes),

$$\hat{V} = Z\hat{I}, \tag{2.1}$$

where $\hat{V}$ and $\hat{I}$ are column vectors of the complex phasor amplitudes of the sinusoidal port voltages and currents. Specifically, the temporally sinusoidally varying voltage $V(t)$ is given in terms of its phasor representation $\hat{V}$ by $V(t) = Re(\hat{V}e^{j\omega t})$.

In defining the S matrix in terms of the Z matrix, we introduce column vectors

of incident ($\hat{a}$) and reflected ($\hat{b}$) wave amplitudes,

$$\hat{a} = (Z_0^{-1/2}\hat{V} + Z_0^{1/2}\hat{I})/2 \tag{2.2}$$

$$\hat{b} = (Z_0^{-1/2}\hat{V} - Z_0^{1/2}\hat{I})/2, \tag{2.3}$$

where Z_0 is a real diagonal matrix whose elements are the characteristic impedances of the transmission line (or wave guide) modes connected to each port. With this definition, the time averaged power delivered to the structure is

$$P = \frac{1}{2}Re\{\hat{I}^\dagger\hat{V}\} = \frac{1}{2}(\hat{a}^\dagger\hat{a} - \hat{b}^\dagger\hat{b}), \tag{2.4}$$

where $\hat{I}^\dagger = (\hat{I}^T)^*$, $\hat{I}^T$ is the transpose of $\hat{I}$, and $*$ denotes complex conjugate.

The scattering matrix S gives the reflected waves in terms of the incident waves, $\hat{b} = S\hat{a}$, and is related to the impedance matrix Z by substituting

$$\hat{V} = Z_0^{1/2}(\hat{a} + \hat{b}) \quad \text{and} \quad \hat{I} = Z_0^{-1/2}(\hat{a} - \hat{b}) \tag{2.5}$$

into Eq. (2.1),

$$S = Z_0^{1/2}(Z + Z_0)^{-1}(Z - Z_0)Z_0^{-1/2}. \tag{2.6}$$

If the structure is lossless, then $Z^\dagger = -Z$, S is unitary ($S^{-1} = S^\dagger$), and P=0.

As discussed in the next section, the impedance matrix Z can be expressed in terms of the eigenfunctions and eigenvalues of the closed cavity. We will argue that the elements of the Z matrix can be represented as combinations of random variables with statistics based on the random plane wave hypothesis for the representation of chaotic wave functions, and the Wigner results (1.3, 1.4) for the spacing distribution of the eigenvalues.

2.2 Z Matrix of Two-Dimensional Cavities

We consider a closed cavity with ports connected to it. For specificity, in our numerical work, we consider the particular, but representative, example of the vertically thin cavity shown in Fig. 2.1(a) coupled to the outside via a coaxial transmission cable. Fig. 2.1(b) shows an example of how this cavity might be connected to a transmission line via a hole in the bottom plate. The cavity shape in Fig. 2.1 is of interest here because the concave curvature of the walls insures that typical ray trajectories in the cavity are chaotic. (Fig. 2.1(a) is a quarter of the billiard shown in Fig. 1.2(c).) For our purposes, a key consequence of the chaotic property of the shape in Fig 2.1(a) is that, if we consider the trajectory of a particle bouncing with specular reflection at the walls (equivalently a ray path), then a randomly chosen initial condition (i. e., random in position $\vec{x}$ within the cavity and isotropically random in the orientation θ of the initial velocity vector) always generates an orbit that is *ergodic* within the cavity. In cases such as Fig. 2.1(a) we assume that the previously mentioned hypotheses regarding eigenfunctions and eigenvalue distributions provide a useful basis for deducing the statistical properties of the Z and S matrices, and, in what follows, we investigate and test the consequences of this assumption.

The vertical height h of the cavity is small, so that, for frequencies of interest, the only propagating waves inside the cavity have electric fields that are purely vertical,

$$\vec{E} = E_z(x, y)\hat{z}. \tag{2.7}$$

This electric field gives rise to a charge density on the top plate $\rho_s = -\epsilon_0 E_z$, and also generates a voltage $V_T(x, y) = -hE_z(x, y)$ between the plates. The magnetic

(a) Top View

(b) Side View of Coupling Details

R1=90cm

R2=63.5cm

21cm

42.5 cm

h=0.2 cm

Inner Radius 0.1 cm

Outer Radius 0.25 cm

Coaxial Transmission Line
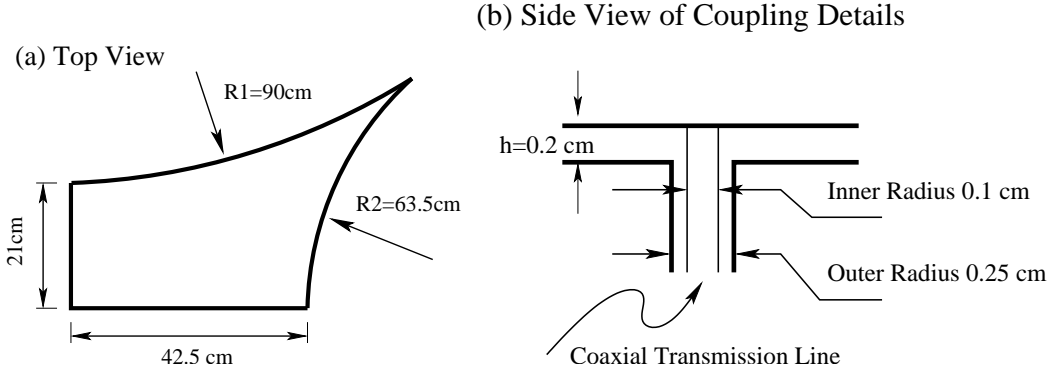
Figure 2.1: (a) Top view of the cavity used in our numerical simulation. (b) Side view of the details of a possible coupling.

field is perpendicular to $\hat{z}$,

$$\vec{B} = (B_x, B_y) = \mu_0 \vec{H}, \tag{2.8}$$

and is associated with a surface current density $\vec{J}_s = \vec{H} \times \hat{z}$ flowing on the top plate.

The cavity excitation problem for a geometry like that in Fig. 2.1(b) is system specific. We will be interested in separating out statistical properties that are independent of the coupling geometry and have a universal (i.e., system-independent) character. For this purpose, we claim that it suffices to consider a simple solvable excitation problem, and then generalize to more complicated cases, such as the coupling geometry in Fig. 2.1(b). Thus we consider the closed cavity (i.e., with no losses or added metal), with localized current sources resulting in a current density $\vec{J}_s(x, y, t) = \sum_i I_i(t) u_i(x, y) \hat{z}$ between the plates. The profile functions $u_i(x, y)$ are assumed to be localized; i.e., $u_i(x, y)$ is essentially zero for $(x - x_i)^2 + (y - y_i)^2 > l_i^2$, where l_i is much smaller than the lateral cavity dimension. $u_i(x, y)$ characterizes the distribution of vertical current at the loca-

tion of the i-th model input (analogous to the i-th transmission line connected to the cavity, although, for this model there are no holes in the upper or lower plates). The profile is normalized such that

$$\int dx dy u_i(x, y) = 1. \tag{2.9}$$

For the sake of simplicity, we only consider the single port case in this section (i.e., there is only one localized source and we may thus drop the subscript i on $u_i(x, y)$). The injection of current serves as a source in the continuity equation for surface charge, $\partial \rho_s / \partial t + \nabla \cdot \vec{J}_s = I u(x, y)$, where $\nabla = (\partial / \partial x, \partial / \partial y)$. Expressed in terms of fields, the continuity equation becomes:

$$\frac{\partial}{\partial t}(-\epsilon_0 E_z) + \nabla \cdot (\tilde{H} \times \hat{z}) = I u(x, y). \tag{2.10}$$

Differentiating Eq. (2.10) with respect to t and using Faraday's law, we obtain,

$$\frac{\partial^2}{\partial t^2}(-\epsilon_0 E_z) + \nabla \cdot \frac{1}{\mu_0} \nabla E_z = u(x, y) \frac{\partial I}{\partial t}. \tag{2.11}$$

Expressing the electric field in terms of the voltage $V_T = -E_z h$, we arrive at the driven wave equation,

$$\frac{1}{c^2} \frac{\partial^2}{\partial t^2} V_T - \nabla^2 V_T = h \mu_0 u \frac{\partial I}{\partial t}, \tag{2.12}$$

where c is speed of light, $c^2 = 1/(\mu_0 \epsilon_0)$.

Assuming sinusoidal time dependence $e^{j\omega t}$ for all field quantities, we obtain the following equation relating $\hat{V}_T$ and $\hat{I}$, the phasor amplitudes of the voltage between the plates and the port current,

$$(\nabla^2 + k^2)\hat{V}_T = -j\omega h \mu_0 u \hat{I} = -jkh\eta_0 u \hat{I}, \tag{2.13}$$

where $\eta_0 = \sqrt{\mu_0/\epsilon_0}$ is the characteristic impedance of free space and $k = \omega/c$. Thus Eq. (2.13) represents a wave equation for the voltage between the plates excited by the input current.

20

To complete our description and arrive at an expression of the form of Eq. (2.1), we need to determine the port voltage V. We take its definition to be a weighted average of the spatially dependent voltage $V_T(x, y, t)$,

$$V = \int dx dy u(x, y) V_T(x, y, t). \tag{2.14}$$

This definition is chosen because it then follows from Eq. (2.10) that the product IV gives the rate of change of field energy in the cavity, and thus Eq. (2.14) provides a reasonable definition of port voltage. Solution of Eq. (2.13) and application of (2.14) to the complex phasor amplitude $\hat{V}_T$ provide a linear relation between $\hat{V}$ and $\hat{I}$, which defines the impedance Z.

To solve Eq. (2.13), we expand $\hat{V}_T$ in the basis of the eigenfunctions of the closed cavity, i.e., $\hat{V}_T = \sum_n c_n \phi_n$, where $(\nabla^2 + k_n^2)\phi_n = 0$, $\int \phi_i \phi_j dx dy = \delta_{ij}$ and $\phi_n(x, y) = 0$ at the cavity boundary. Thus, multiplying Eq. (2.13) by ϕ_n and integrating over (x, y) yields

$$c_n(k^2 - k_n^2) = -jkh\eta_0 \langle u\phi_n \rangle \hat{I}, \tag{2.15}$$

where $k_n = \omega_n/c$, ω_n is the eigenfrequency associated with ϕ_n, and $\langle u\phi_n \rangle = \int \phi_n u dx dy$. Solving for the coefficients c_n and computing the voltage $\hat{V}$ yields

$$\hat{V} = -j \sum_n \frac{kh\eta_0 \langle u\phi_n \rangle^2}{k^2 - k_n^2} \hat{I} = Z\hat{I}. \tag{2.16}$$

This equation describes the linear relation between the port voltage and the current flowing into the port. Since we have assumed no energy dissipation so far (e.g., due to wall absorption or radiation), the impedance of the cavity is purely imaginary, as is indicated by Eq. (2.16).

The expression for Z in Eq. (2.16) is equivalent to a formulation introduced by Wigner and Eisenbud [41] in nuclear-reaction theory in 1947, which was generalized and reviewed by Lane and Thomas [42], and Mahaux and Weidenmüller

21

[43]. Recently, a supersymmetry approach to scattering based on this formulation was introduced by Verbaarschot et.al. [44] and further developed by Lewenkopf [45] and Fyodorov [46](which they called the "K-matrix" formalism), and it has also been adapted to quantum dots by Jalabert, Stone and Alhassid [47].

2.3   Statistical Representation

Explicit evaluation of Eq. (2.16) in principle requires determination of the eigenvalues and corresponding eigenfunctions of the closed cavity. We do not propose to do this. Rather, we adopt a statistical approach to the properties of eigenfunctions of chaotic systems, and we use this to construct models for the statistical behavior of the impedance. By a statistical approach we mean the following. For high frequencies such that $k = \omega/c \gg L^{-1}$ where L is a typical dimension of the cavity, the sum in Eq. (2.16) will be dominated by high order (short wavelength) modes with $k_n L \gg 1$. For these modes the precise values of the eigenvalues k_n as well as the overlap integrals $\langle u\phi_n \rangle$ will depend sensitively on the geometry of the cavity. Rather than predict these values precisely we will replace them with random variables. The assumption here is that there are many modes with k_n in the narrow interval δk centered at k (where $\Delta \ll (\delta k)^2 \ll k^2$), and, if we choose one of these at random, then its properties can be described by a statistical ensemble. As discussed in Chapter 1, the properties of the short wavelength eigenfunctions can be understood in terms of ray trajectories. For geometries like that in Fig. 2.1(a), ray trajectories are chaotic.

A particularly successful approach to describe the statistical properties of the eigenfunctions of chaotic billiards, dating back to Berry [48], assumes that at any point not too close to the boundary the wave function has statistical properties

similar to those of a random superposition of many plane waves,

$$\phi_n(\vec{x}) \simeq \sum_{j=1}^{N} \alpha_j \exp(ik_n\vec{e}_j \cdot \vec{x} + i\beta_j), \qquad N \gg 1, \qquad (2.17)$$

where the modulus k_n of the incoming waves is fixed, but directions $\vec{e}_j$, amplitude α_j and the phase β_j are independent random variables. In systems with time-reversal symmetry, there is an additional restriction that the wave function has to be real. Equation (2.17) cannot be strictly true near billiard boundaries, but this occurs only in a relatively small volume since it is assumed that the wavelength is small compared to the cavity size.

The wave orientation in Eq. (2.17) is uniformly distributed, and the phase is also uniformly distributed in $[0, 2\pi]$. Since the summation is over a large number N, and the magnitude α_j have the same distribution for all the plane waves, one expects a Gaussian distribution for the wave function amplitude $\phi_n(\vec{x})$, and we an calculate the overlap integral $\langle u\phi_n \rangle$ appearing in the numerator of (2.16). The central limit theorem implies that the overlap integral will be a Gaussian random variable with zero mean. The variance of the overlap integral can be obtained using Eq. (2.17),

$$E\{\langle u\phi_n \rangle^2\} = \frac{1}{A} \int_0^{2\pi} \frac{d\theta}{2\pi} |\bar{u}(\vec{k}_n)|^2, \qquad (2.18)$$

where $E\{.\}$ denotes expected value, and $\bar{u}(\vec{k}_n)$ is the Fourier transform of the profile function $u(x, y)$,

$$\bar{u}(\vec{k}_n) = \int dxdy u(x, y) exp(-i\vec{k}_n \cdot \vec{x}), \qquad (2.19)$$

and $\vec{k}_n = (k_n \cos\theta, k_n \sin\theta)$. The integral in (2.18) over θ represents averaging over the directions $\vec{e}_j$ of the plane waves.

The variance of $\langle u\phi_n \rangle$ depends on the eigenvalue k_n^2. If we consider a localized source $u(x, y)$ such that the size of the source is less than the typical wavelength

$2\pi/k_n$, then the variance will be A^{-1} (recall the normalization of u given by Eq. (2.9)). As larger values of k_n are considered, the variance ultimately decreases to zero. As an illustrative example, suppose that the source corresponds to an annular ring of current of radius a,

$$u(x,y) = \frac{1}{\pi}\delta(x^2 + y^2 - a^2). \tag{2.20}$$

In this case, one finds from Eq. (2.18),

$$E\{\langle u\phi_n\rangle^2\} = A^{-1}J_0^2(k_n a), \tag{2.21}$$

which decreases to zero with increasing $k_n a$ as $(k_n a)^{-1}$. (A smooth, analytic function $u(x,y)$ will yield a sharper cutoffs in variance as k_n increases.)

Modelling of Eq. (2.16) also requires specifying the distribution of eigenvalues k_n appearing in the denominator. According to the Weyl's formula (1.1) for a two dimensional cavity of area A, the average separation between adjacent eigenvalues, $k_n^2 - k_{n-1}^2$, is $4\pi A^{-1}$. The distribution of spacings of adjacent eigenvalues is predicted to have the characteristic Wigner form for cavities with chaotic trajectories. In particular, defining the normalized spacing, $s_n = A(k_n^2 - k_{n-1}^2)/4\pi$, the probability density function for s_n is predicted to be closely approximated by Eq. (1.3) for chaotic systems with time-reversal symmetry. We will generate values for the impedance assuming that sequences of eigenvalues can be generated from a set of separations s_n which are independent and distributed according to Eq. (1.3). The usefulness of the assumption of the independence of separations will have to be tested, as it is known that there are long range correlations in the spectrum, even if nearby eigenvalues appear to have independent spacings. Our assertion is that the sum in Eq. (2.16) is determined mainly by the average spacing and the distribution of separations of eigenvalues for k_n near k and that

long range correlations in the k_n are unimportant.

2.4   Cavity Impedance and Radiation Impedance

Combining our expressions for $\langle u\phi_n \rangle$ and using the result that for a two dimensional cavity the mean spacing between adjacent eigenvalues is $\Delta = 4\pi A^{-1}$, the expression for the cavity impedance given in Eq. (2.16) can be rewritten,

$$Z = -\frac{j}{\pi} \sum_{n=1}^{\infty} \Delta \frac{R_R(k_n)w_n^2}{k^2 - k_n^2}, \tag{2.22}$$

where w_n is taken to be a Gaussian random variable with zero mean and unit variance, the k_n are distributed according to Eq. (1.3), and R_R is given by

$$R_R(k) = \frac{kh\eta_0}{4} \int \frac{d\theta}{2\pi} |u(\vec{k})|^2. \tag{2.23}$$

Our rationale for expressing the impedance in the form of Eq. (2.22) and introducing $R_R(k_n)$ is motivated by the following observation. Suppose we allow the lateral boundaries of the cavity to be moved infinitely far from the port. That is, we consider the port as a 2D free-space radiator. In this case, we solve Eq. (2.13) with a boundary condition corresponding to outgoing waves, which can be readily done by the introduction of Fourier transforms. This allows us to compute the phasor port voltage $\hat{V}$ by Eq. (2.14). Introducing a complex radiation impedance $Z_R(k) = \hat{V}/\hat{I}$ (for the problem with the lateral boundaries removed), we have

$$Z_R(k) = -\frac{j}{\pi} \int_0^{\infty} \frac{dk_n^2}{k^2 - k_n^2} R_R(k_n), \tag{2.24}$$

where $R_R(k_n)$ is given by Eq. (2.23) and k_n is now a continuous variable. The impedance $Z_R(k)$ is complex with a real part obtained by deforming the k_n integration contour to pass above the pole at $k_n = k$. This follows as a consequence

of applying the outgoing wave boundary condition, or equivalently, letting k have a small negative imaginary part. Thus, we can identify the quantity $R_R(k)$ in Eq. (2.23) as the radiation resistance of the port resulting from one half the residue of the integral in (2.24) at the pole, $k^2 = k_n^2$,

$$Re[Z_R(k)] = R_R(k), \qquad (2.25)$$

and $X_R(k) = Im[Z_R(k)]$ is the radiation reactance given by the principal part (denoted by P) of the integral (2.24),

$$X_R(k) = P\{-\frac{1}{\pi}\int_0^\infty \frac{dk_n^2}{k^2 - k_n^2} R_R(k_n)\}. \qquad (2.26)$$

As an example, we evaluate this radiation impedance for the case of the annular current profile (2.20) in Appendix A and find

$$\bar{Z} = -j(kh\eta/4)J_0(ka)Y_0(ka), \qquad (2.27)$$

where Y_0 is a Bessel function of the second kind. This impedance has a positive imaginary logarithmic divergence as $ka \to 0$ which is due to the large inductance associated with feeding the current through a small circle of radius a.

Based on the above, the connection between the cavity impedance, represented by the sum in Eq. (2.22), and the radiation impedance, represented in Eq. (2.25) and Eq. (2.26), is as follows. The cavity impedance, Eq. (2.22), consists of a discrete sum over eigenvalues k_n with weighting coefficients w_n which are Gaussian random variables. There is an additional weighting factor $R_R(k_n)$ in the sum, which is the radiation resistance. The radiation reactance, Eq. (2.26), has a form analogous to the cavity impedance. It is the principle part of a continuous integral over k_n with random coupling weights set to unity. While, Eqs. (2.22), (2.25), (2.26), have been obtained for the simple model input $\hat{J} = \hat{I}u(x,y)$ in

$0 \leq z \leq h$ with perfectly conducting plane surfaces at $z = 0, h$, we claim that these results apply in general. That is, for a case like that in Fig. 2.1(b), $Z_R(k)$ (which for the simple model is given by Eq. (2.24)) can be replaced by the radiation impedance for the problem with the same geometry. It is important to note that, while $R_R(k)$ is nonuniversal (i.e., depends on the specific coupling geometry, such as that in Fig. 2.1(b)), it is sometimes possible to independently calculate it, and it is also a quantity that can be directly measured (e.g., absorber can be placed adjacent to the lateral walls). In the next chapter, we will use the radiation impedance to normalize the cavity impedance yielding a universal distribution for the impedance of a chaotic cavity.

Chapter 3

Impedance Statistics: One Port Lossless Case

3.1 Introduction

In the lossless case, the impedance of the cavity Z in Eq. (2.22) is a purely imaginary number and S, the reflection coefficient, is a complex number with unit modulus. Terms in the summation of Eq. (2.22) for which k^2 is close to k_n^2 will give rise to large fluctuations in Z as either k^2 is varied or as one considers different realizations of the random numbers. The terms for which k^2 is far from k_n^2 will contribute to a mean value of Z. Accordingly, we write

$$Z = \bar{Z} + \tilde{Z}, \tag{3.1}$$

where $\bar{Z}$, the mean value of Z, is written as

$$\bar{Z} = -\frac{j}{\pi} \sum_n \Delta E\{\frac{R_R(k_n^2)}{k^2 - k_n^2}\}, \tag{3.2}$$

and we have used the fact that the w_n^2 are independent with $E\{w_n^2\} = 1$. If we approximate the summation in Eq. (3.2) by an integral, noting that Δ is the mean spacing between eigenvalues, comparison with (2.26) yields

$$\bar{Z} = jX_R(k), \tag{3.3}$$

where $X_R = Im[Z_R]$ is the radiation reactance defined by Eq. (2.26). Thus, the mean part of the fluctuating impedance of a closed cavity is equal to the radiation reactance that would be obtained under the same coupling conditions for an antenna radiating freely; i.e., in the absence of multiple reflections of waves from the lateral boundaries of the cavity. The equivalent conclusion for the radiation scattering coefficient is evident from the treatment of Brouwer [49].

We now argue that, if k^2 is large enough that many terms in the sum defining Z satisfy $k_n^2 < k^2$, then the fluctuating part of the impedance $\tilde{Z}$ has a Lorentzian distribution with a characteristic width $R_R(k)$. That is, we can write

$$Z = j(X_R + R_R \xi), \qquad (3.4)$$

where ξ is a zero mean unit width Lorentzian distributed random variable, $P_\xi(\xi) = [\pi(1 + \xi^2)]^{-1}$.

Lorentzian distribution appears in the theory of nuclear scattering [50] and arises as consequences of random matrix theory [46, 51]. That the characteristic width scales as $R_R(k)$ follows from the fact that the fluctuating part of the impedance is dominated by terms for which $k_n^2 \simeq k^2$. The size of the contribution of a term in the sum in Eq. (2.22) decreases as $|k^2 - k_n^2|$ in the denominator increases. The many terms with large values of $|k^2 - k_n^2|$ contribute mainly to the mean part of the reactance with the fluctuations in these terms cancelling one another due to the large number of such terms. The contributions to the mean part from the relatively fewer terms with small values of $|k^2 - k_n^2|$ tend to cancel due to the sign change of the denominator while their contribution to the fluctuating part of the reactance is significant since there are a smaller number of these terms. Consequently, when considering impedance fluctuations, it suffices to treat $R_R(k_n)$ as a constant in the summation in Eq. (2.22) and factor it out.

This results in a sum that is independent of coupling geometry and is therefore expected to have a universal distribution.

3.2 Numerical Results for a Model Normalized Impedance

To test the arguments above, we consider a model normalized cavity reactance $\xi = X/R_R$ and also introduce a normalized wavenumber $\tilde{k}^2 = k^2/\Delta = k^2 A/4\pi$. In terms of this normalized wavenumber, the average of the eigenvalue spacing [average of $(\tilde{k}_{n+1}^2 - \tilde{k}_n^2)$] is unity. Our model normalized reactance is

$$\xi = -\frac{1}{\pi} \sum_{n=1}^{N} \frac{w_n^2}{\tilde{k}^2 - \tilde{k}_n^2}, \tag{3.5}$$

where the w_n are independent Gaussian random variables, $\tilde{k}_n^2$ are chosen according to various distributions, and we have set $R_R(k_n)$ to a constant value for $n \leq N$ and $R_R(k_n) = 0$ for $n > N$. The fluctuating part of $j\xi$ given by Eq. (3.5) mimics the fluctuating part of the impedance Z in the case in which $R_R(k_n)$ has a sharp cut-off for eigenmodes with $n > N$. In terms of ξ, Eq. (3.4) becomes

$$P_\xi(\xi) = \frac{1}{\pi} \frac{1}{[(\tilde{\xi} - \bar{\xi})^2 + 1]}, \tag{3.6}$$

where $\bar{\xi}$ is the mean of ξ.

First we consider the hypothetical case where the collection of $\tilde{k}_n^2$ values used in Eq. (3.5) result from N independent and uniformly distributed random choices in the interval $0 \leqslant \tilde{k}_n^2 \leqslant N$. In contrast to Eq. (1.3), this corresponds to a Poisson distribution of spacings $P(s) = exp(-s)$ for large N. This case is analytically solvable (see Appendix B) and that the mean value $\bar{\xi}$ is

$$\bar{\xi} = P\{-\frac{1}{\pi} \int_0^N \frac{d\tilde{k}_n^2}{\tilde{k}^2 - \tilde{k}_n^2}\} = \frac{1}{\pi} ln|\frac{N - \tilde{k}^2}{\tilde{k}^2}|, \tag{3.7}$$

30

and, furthermore, that ξ has a Lorentzian distribution.

Our next step is to numerically determine the probability distribution function for ξ given by (3.5) in the case where the spacing distribution corresponds to the TRS case described by Eq. (3). We generated 10^6 realizations of the sum in Eq. (3.5). For each realization we randomly generated $N = 2000$ eigenvalues using the spacing probability distribution (3), as well as $N = 2000$ random values of w_n chosen using a Gaussian distribution for w_n with $E\{w_n\} = 0$ and $E\{w_n^2\} = 1$. We first test the prediction of Eq. (3.7) by plotting the median value of ξ versus $\tilde{k}^2$ in Fig. 3.1(a). (We use the median rather than the mean, since, for a random variable with a Lorentzian distribution, this quantity is more robust when a finite sample size is considered.) Also plotted in Fig. 3.1(a) is the formula (3.7). We see that the agreement is very good. Next we test the prediction for the fluctuations in ξ by plotting a histogram of ξ values for the case $\tilde{k}^2 = N/2$ in Fig. 3.1(b). From (3.7) for $\tilde{k}^2 = N/2$ the mean is expected to be zero, and, as can be seen in the figure, the histogram (open circles) corresponds to a Lorentzian with zero mean and unit width (solid line) as expected. Histograms plotted for other values of $\tilde{k}^2$ agree with the prediction but are not shown. Thus, we find that the statistics of ξ are the same for $P(s) = exp(-s)$ (Poisson) and for $P(s)$ given by Eq. (1.3). Hence we conclude that the statistics of ξ are independent of the distribution of spacings. This is further supported by Fig. 3.1(c) where the histogram of ξ for $\tilde{k}^2 = N/2$ is plotted for the case in which the spacing distribution is that corresponding to time reversal symmetry broken (TRSB) systems. (the TSRB case will be discussed more carefully in a subsequent chapter). Again the histogram is in excellent agreement with (3.6). This implies that, for the lossless case, with a single input transmission line to the cavity, the impedance statistics are not so

31

sensitive to the spacing distributions, as long as they have the same mean value.

In principle, one can also incorporate additional eigenvalue correlation from random matrix theory in the statistics generating the k_n^2 in Eq. (3.5).(and when losses are considered, this is necessary.) We note that the mean and width of the distribution in the random matrix approach are specific to the random matrix problem. In contrast, in our formulation, these quantities are determined by the geometry specific port coupling to the cavity through the radiation impedance $Z_R(k_n^2)$.

3.3   HFSS Simulation Result for the Normalized Impedance

To test our prediction for the distribution function of the normalized impedance, we have computed the impedance for the cavity in Fig. 2.1(a) for the coupling shown in Fig. 2.1(b) using the commercially available program HFSS (High Frequency Structure Simulator [52]). To create different realizations of the configuration, we placed a small metallic cylinder of radius 0.6 cm and height h at 100 different points inside the cavity. In addition, for each location of the cylinder, we swept the frequency through a 2.0 GHz range (about 100 modes) from 6.75GHz to 8.75GHz in 4000 steps of width 5×10^{-4} GHz. We generated 100,000 impedance values. In addition, to obtain the radiation impedance, we also used HFSS to simulate the case with radiation boundary conditions assigned to the sidewalls of the cavity. We find that the average value of the cavity reactance (which we predict to be the radiation reactance) has large systematic fluctuations. This is
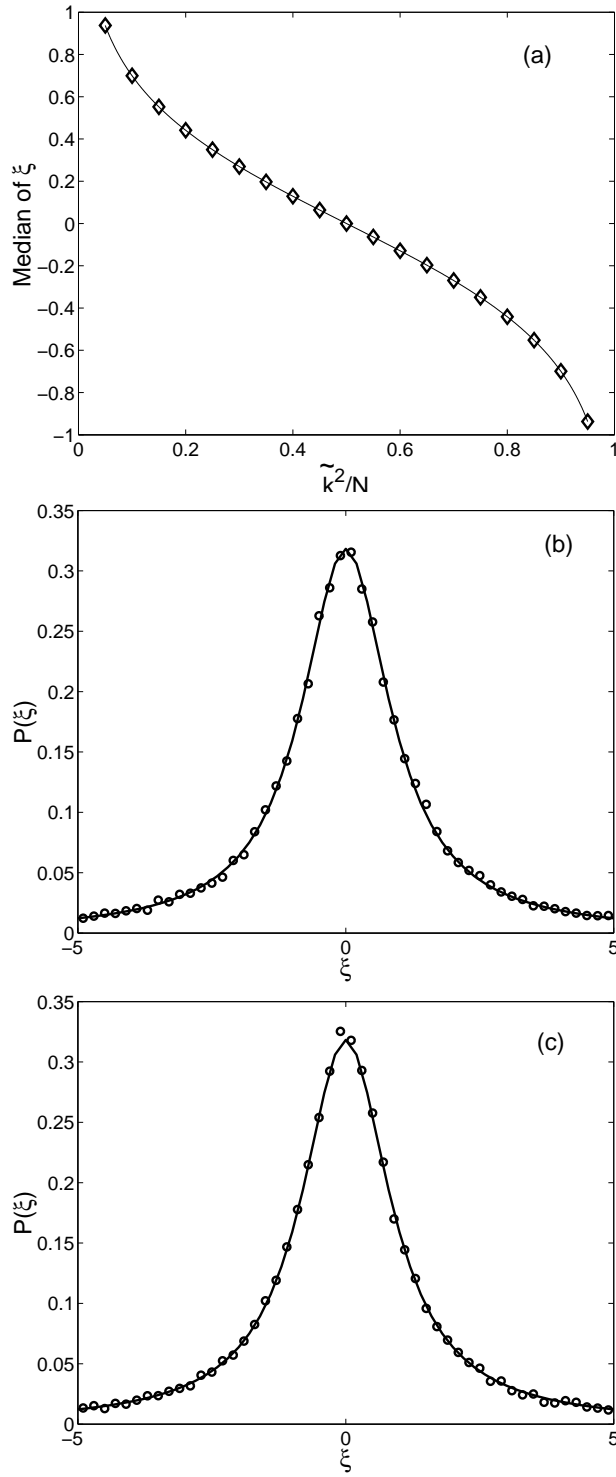
Figure 3.1: (a) Median of ξ versus $\tilde{k}^2/N$, compared with Eq. (3.7). (b) Histogram of ξ (solid dots) in the TRS case compared with a standard Lorentzian (c) Same as (b) but for the TRSB case.
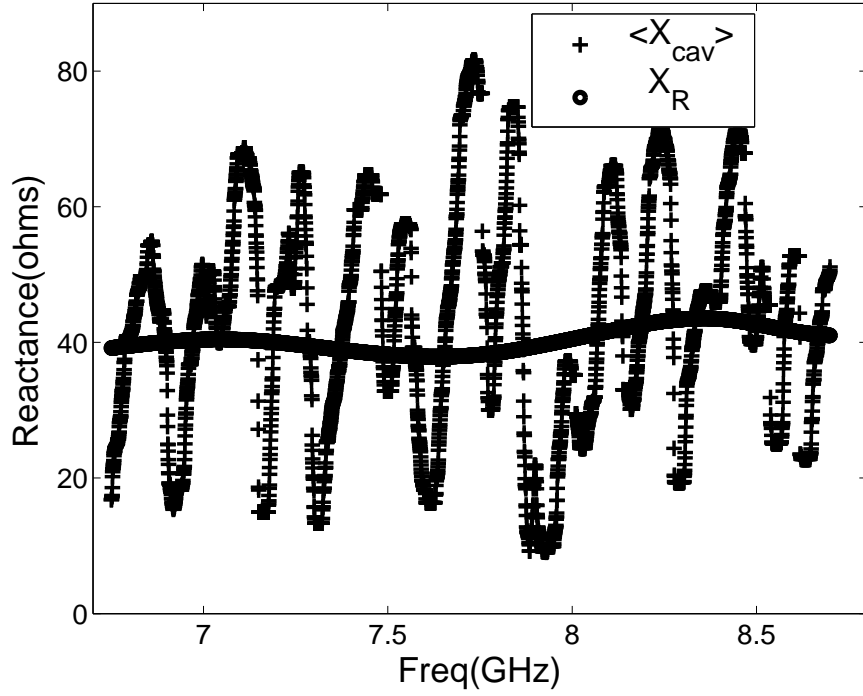
Figure 3.2: Median cavity reactance averaged over 100 realization vs. frequencies ranged from 6.75GHz to 8.75GHz, compared with the corresponding radiation reactance $Im[Z_R(\omega)]$.

illustrated in Fig. 3.2 where we plot the median cavity reactance versus frequency. Here the median is taken with respect to the 100 locations of the perturbing disc. Also shown in Fig. 3.2 is the radiation reactance $X_R(\omega) = Im[Z_R(\omega)]$.

As can be seen the radiation reactance varies only slightly over the plotted frequency range, whereas the median cavity reactance has large frequency dependent fluctuations about this value. On the other hand, we note that over the range 6.75-8.75 GHz, the average radiation reactance is 40.4 Ω and the average of the median cavity reactance is 42.3Ω. Thus over this frequency band, there is good agreement. The scale of the fluctuations in cavity reactance is on the order

of 0.2GHz, which is much larger than the average spacing between cavity resonances which is only 0.016GHz. Thus, these fluctuations are not associated with individual resonances. Rather, the frequency scale of 0.2GHz suggests that they are multipath interference effects ($L \sim 100cm$), which survive in the presence of the moveable conducting disc. One possibility is that the fluctuations are the result of scars [37] and this will be investigated in the future. The implication of Fig. 3.2 is that to obtain good agreement with the theory predicting a Lorentzian distribution, it may be necessary to average over a sufficiently large frequency interval.

To test the Lorentzian prediction we normalize the cavity impedance using the radiation impedance as in Eq. (3.3) and Eq. (3.4), the normalized impedance values, $\xi = \{\mathrm{Im}[Z(k)] - X_R(k)]\}/R_R(k)$, are computed, and the resulting histogram approximations to $P(\xi)$ is obtained. Fig. 3.3(a) shows the result for the case where we have used data in the frequency range 6.75GHz to 8.75GHz (the range plotted in Fig. 3.2). The histogram points are shown as dots, and the theoretical unit width Lorentzian is shown as a solid curve. Good agreement between the predicted Lorentzian and the data is seen. Figures 3.3 (b)-(e) show similar plots obtained for smaller frequency range of width 0.5GHz: (b) 6.75 - 7.25 GHz, (c) 7.25 - 7.75GHz, (d) 7.75 - 8.25 GHz, (e) 8.25 - 8.75 GHz. For these narrow frequency ranges, we see that Figs. 3.3(b) and 3.3(c) show good agreement with (3.6), while, on the other hand, Figs. 3.3(d) and 3.3(e) exhibit some differences. These are possibly associated with the variances in the median cavity reactance shown in Fig. 3.2 as the agreement with the Lorentzian prediction improves when averaging over a large range of frequencies.

35
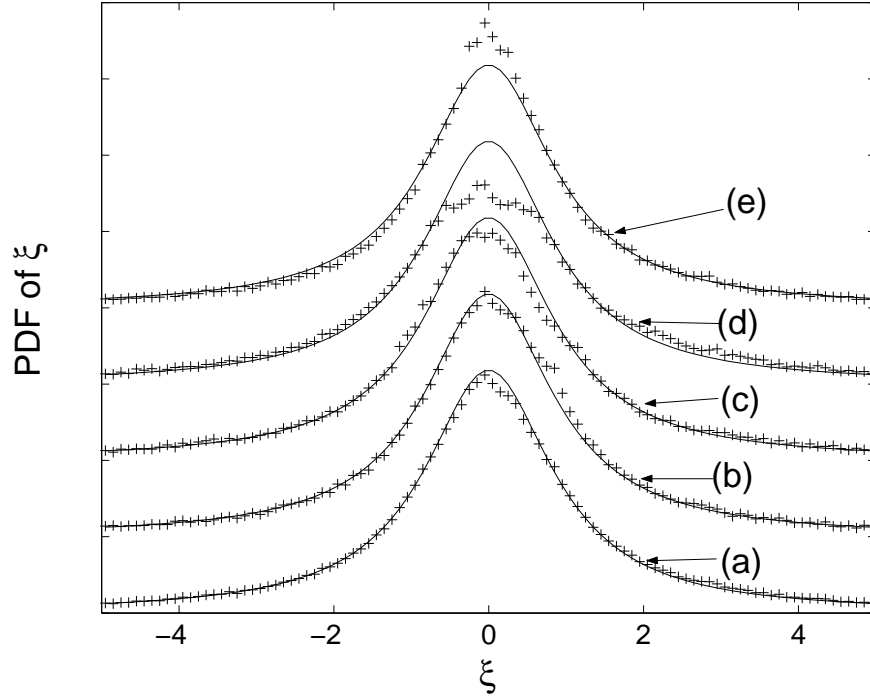
Figure 3.3: Histogram approximation to $P_\xi(\xi)$ from numerical data calculated using HFSS in different frequency ranges. (a) 6.75 - 8.75 GHz, (b) 6.75 - 7.25 GHz, (c) 7.25 - 7.75GHz, (d) 7.75 - 8.25 GHz, (e) 8.25 - 8.75 GHz.
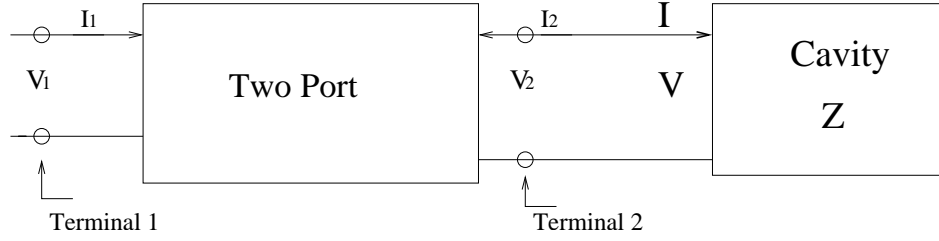
Figure 3.4: Schematic description of the two port extension

3.4 Variation in Coupling

In this section, we bolster our arguments connecting the radiation impedance and the normalization of the cavity impedance by showing that the relation is preserved when the details of the coupling port are modified. Let us consider a one-port coupling case in which the actual coupling is equivalent to the cascade of a lossless two port and a "pre-impedance" Z seen at terminal 2, as illustrated in Fig. 3.4.

The impedance Z at terminal 2 then transforms to a new impedance Z' at terminal 1 of the two port according to

$$Z' = j\hat{X}_{11} + \frac{\hat{X}_{12}\hat{X}_{21}}{j\hat{X}_{22} + Z}, \tag{3.8}$$

where $j\hat{X}_{ij}$ is now the purely imaginary 2 by 2 impedance matrix of the lossless two-port. We now ask how Z transforms to Z' when (a) Z is the complex impedance Z_R corresponding to the radiation impedance into the cavity (i.e. the cavity boundaries are extended to infinity) and (b) $Z = jX$ is an imaginary impedance corresponding to a lossless cavity, where X has a mean $\bar{X}$ and Lorentzian distributed fluctuation $\tilde{X}$.

First considering case (a) the complex cavity impedance $Z_R = R_R + jX_R$

transforms to a complex impedance $Z'_R = R'_R + jX'_R$ where

$$R'_R = R_R \frac{\hat{X}_{12}\hat{X}_{21}}{R_R^2 + (\hat{X}_{22} + X_R)^2}, \tag{3.9}$$

and

$$X'_R = \hat{X}_{11} - (\hat{X}_{22} + X_R)\frac{\hat{X}_{12}\hat{X}_{21}}{R_R^2 + (\hat{X}_{22} + X_R)^2}. \tag{3.10}$$

In case (b) we consider the transformation of the random variable X to a new random variable X' according to $X' = \hat{X}_{11} + \hat{X}_{12}\hat{X}_{21}/(\hat{X}_{22} + X)$. One can show that if X is Lorentzian distributed with mean X_R and width R_R then X' will be Lorentzian distributed with mean X'_R and the width R'_R. Thus, the relation between the radiation impedance and the fluctuating cavity impedance is preserved by the lossless two port. Accordingly, we reassert that this relation holds in general for coupling structures whose properties are not affected by the distant walls of the cavity. A treatment similar to that above has also been given by Brouwer [49] in the context of scattering with a scattering matrix description of the connection between terminal 1 and 2.

We now summarize the main ideas of this chapter. The normalized impedance of a lossless chaotic cavity with time-reversal symmetry has a universal distribution which is a Lorentzian. The width of the Lorentzian and the mean value of the impedance can be obtained by measuring the corresponding radiation impedance under the same coupling conditions [54]. The physical interpretation of this correspondence is as follows. In the radiation impedance, the imaginary part is determined by the near field, which is independent of cavity boundaries. On the other hand, the real part of the radiation impedance is related to the far field. In a closed, lossless cavity, the real part of the impedance vanishes. However, waves that are radiated into the cavity are reflected from the bound-

38

aries eventually returning to the port and giving rise to fluctuation in the cavity reactance.

Chapter 4

Generalization: The Statistics of Z Matrices

In the previous two chapters, we restricted our considerations to discussion of the simplest case, that of a one-port, time-reversal symmetric, lossless cavity. In this chapter, we will generalize our model to describe the impedance matrix in more complicated situations. The implications of our theory for scattering matrices are discussed in chapter 5.

4.1 Lossless Multiport Case with Time Reversal Symmetry

Following the one-port discussion in previous chapter, we consider a quasi-two dimensional cavity in which only the lowest order transverse magnetic modes are excited. The fields in the cavity are determined by the spatially dependent phasor amplitude of the voltage $\hat{V}_T(x, y)$. In contrast to Eq. (2.13), the voltage in the multi-port case is excited by currents $\hat{I}_i$ driving at the various coupling ports,

$$(\nabla_\perp^2 + k^2)\hat{V}_T = -jkh\eta_0 \sum_{i=1}^{M} u_i \hat{I}_i. \qquad (4.1)$$

Here $k = \omega/c$, $\eta_0 = \sqrt{\mu_0/\epsilon_0}$, h is the height of the cavity and an exponential time dependence $\exp(j\omega t)$ has been assumed for all time dependent quantities. Each of the M ports is characterized by a profile function u_i centered at different locations and $\int dx dy u_i = 1$. The phasor voltage at each port can be calculated as before, $\hat{V}_i = \int dx dy u_i \hat{V}_T \equiv < u_i \hat{V}_T >$ and is linearly related to the phasor currents $\hat{I}_j$ through the impedance matrix, $\hat{V}_i = \sum_j Z_{ij} \hat{I}_j$.

To obtain an expression for the matrix Z, we expand $\hat{V}_T$ as before in the basis ϕ_n, the eigenfunctions of the closed cavity [55]. The result is

$$Z = -jkh\eta_0 \sum_n \frac{\Phi_n \Phi_n^T}{k^2 - k_n^2}, \tag{4.2}$$

where the vector Φ_n is $[\langle u_1 \phi_n \rangle, \langle u_2 \phi_n \rangle,...,\langle u_M \phi_n \rangle]^T$. Using the random eigenfunction hypothesis, we write ϕ_n as a superposition of random plane waves. Thus the elements of the M-dimensional vector Φ_n will be Gaussian random variables with zero mean. Elements of Φ_n with different values of n corresponding to different eigenfunctions will be independent. However, for a given eigenfunction the elements of Φ_n may be correlated. This will be true, particularly, if two ports are close together, because the random superposition of plane waves leads to an autocorrelation function $J_0(k\delta r)$ at two positions separated by δr [56]. To treat correlations we write

$$\Phi_n = L(k_n)w_n, \tag{4.3}$$

where L is a non-random, as yet unspecified, $M \times M$ matrix that depends on the specific coupling geometry at the ports and may depend smoothly on k_n, and w_n is an M-dimensional Gaussian random vector with zero mean and covariance matrix equal to the $M \times M$ identity matrix. That is we require that the components of the random vector w_n are statistically independent of each

other, each with unit variance. Correlations between ports are described by the off-diagonal components of L. The idea behind (4.3) is that the excitation of the ports by an eigenmode will depend on the port geometry and on the structure of the eigenmode in the vicinity of the ports. The dependence on the specific port geometry is not sensitive to small changes in the frequency or cavity configuration and is embodied in the matrix quantity $L(k)$. The structure of the eigenmode in the vicinity of the ports, however, is very sensitive to the frequency and cavity configuration, and this motivates the statistical treatment via the random plane wave hypothesis. From the random plane wave hypothesis, the excitation of the port from a given plane wave component is random, and, since many such waves are superposed, by the central limit theorem, the port excitation is a Gaussian random variable, as reflected by the vector w_n. In the previous chapter, we have derived a result equivalent to (4.3) for the case of a one-port with a specific model of the excitation at the port (namely, a vertical source current density $Iu(x, y)\hat{z}$ between the plates). Our derivation here will be more general in that it does not depend on a specific excitation or on the two-dimensional cavity configuration used in the previous chapter. Thus this derivation applies, for example, to three dimensional cavities, and arbitrary port geometries. From (4.2) and (4.3) we have for the Z matrix

$$Z = -jkh\eta_0 \sum_n \frac{L(k_n)w_n w_n^T L^T(k_n)}{k^2 - k_n^2}.$$ (4.4)

We now take the continuum limit of (4.4) and average over w_n,

$$\langle Z \rangle = -j \int_0^\infty kh\eta_0 L(k') \frac{\langle w_n w_n^T \rangle}{k^2 - (k')^2} L^T(k') \frac{dk'^2}{\Delta},$$ (4.5)

where Δ is the averaged spacing in k_n^2 values. We note that the continuum limit is approached as the size of the cavity is made larger and larger, thus making the resonance spacing $(k_{n+1}^2 - k_n^2)$ approach zero. Thus, the continuum

limit corresponds to moving the lateral walls of the cavity to infinity. Using our previous one-port argument as a guide, we anticipate that, if the pole in Eq. (4.5) at $k'^2 = k^2$ is interpreted in the causal sense (corresponding to outgoing waves in the case with the walls removed to infinity), then $\langle Z \rangle$ in (4.5) is the radiation impedance matrix,

$$\langle Z \rangle = Z_R(k) = \hat{R}_R(k) + j\hat{X}_R(k), \tag{4.6}$$

where $\hat{V} = Z_R(k)\hat{I}$ with $\hat{V}$ the M-dimensional vector of port voltages corresponding to the M-dimensional vector of port currents $\hat{I}$, in the case where the lateral walls have been removed to infinity. With the above interpretation of the pole, the real part of Eq. (4.5) yields

$$\hat{R}_R(k) = \pi k h \eta_0 L(k) L^T(k)/\Delta. \tag{4.7}$$

Thus, Eq. (4.2) becomes

$$Z = -\frac{j}{\pi} \sum_n \Delta \frac{\hat{R}_R^{1/2}(k_n) w_n w_n^T \hat{R}_R^{1/2}(k_n)}{k^2 - k_n^2}, \tag{4.8}$$

where $\langle w_n w_n^T \rangle = 1_M$. (Note that the formula for Δ is different in two and three dimensions.) In the case of transmission line inputs that are far apart, e.g., of the order of the cavity size, then the off-diagonal elements of Z_R are small and can be neglected. On the other hand, this will not be the case if some of the transmission line inputs are separated from each other by a short distance of the order of a wavelength. Similarly, if there is a waveguide input to the cavity where the waveguide has multiple propagating modes, then there will be components of $\hat{V}$ and $\hat{I}$ for each of these modes, and the corresponding off-diagonal elements of Z_R for coupling between these modes will not be small.

For the remainder of this chapter, we will assume identical transmission line inputs that are far enough apart that we may neglect the off-diagonal elements of

Z_R. As before, we will take the eigenvalues k_n^2 to have a distribution generated by Random Matrix Theory. Because the elements of Z depend on the eigenvalues k_n^2, there will be correlations among the elements. In the lossless case the elements of the Z matrix are imaginary, $Z = jX$, where X is a real symmetric matrix. Consequently X has real eigenvalues. We will show in the next section that the distribution for individual eigenvalues of X is Lorentzian with mean and width determined by the corresponding radiation impedance.

4.2 Effects of Time-Reversal Symmetry Breaking (TRSB)

In the time-reversal symmetric system, the eigenfunctions of the cavity are real and correspond to superpositions of plane waves with equal amplitude waves propagating in opposite directions (2.17). If a non-reciprocal element (such as a magnetized ferrite) is added to the cavity, then time reversal symmetry is broken (TRSB). As a consequence, the eigenfunctions become complex. Eq. (2.17) is modified by removal of the operation of taking the real part, and the $\langle u\phi_n \rangle$ in Eq. (2.22) also become complex. In practice, there exists a crossover regime for the transition from situations where time reversal symmetry applies to those it is fully-broken. An interested reader might refer to situations where discussion in Ref. [36] and the references therein. However, in this chapter, we will discuss only the case when time-reversal symmetry is fully broken. In this case we find

$$\langle u_\ell \phi_n \rangle = [\Delta \hat{R}_R(k_n)]^{1/2} w_{\ell n} \tag{4.9}$$

where $w_{\ell n} = (w_{\ell n}^{(r)} + j w_{\ell n}^{(i)})/\sqrt{2}$ and $w_{\ell n}^{(r)}$ and $w_{\ell n}^{(i)}$ are real, independent Gaussian random variables with zero mean and unit variance. The extra factor of $\sqrt{2}$

accounts for the change in the normalization factor in Eq. (2.17), required when the eigenfunctions become complex. Further, transpose w_n^T, in Eq. (4.8) is now replaced by the conjugate transpose $w_n^\dagger$.

A further consequence of TRSB is that the distribution of eigenvalues is changed. The main difference is the behavior of $P(s)$ for small s. In particular, the probability of small spacings in a TRSB system $(P(s) \sim s^2)$ is less than than of a TRS system $(P(s) \sim s)$.

For the sake of simplicity, we will assume all the transmission lines feeding the cavity ports are identical, and have the same radiation impedance, $Z_R = \hat{R}_R + j\hat{X}_R = (R_R + jX_R)1_M$, where R_R and X_R are real scalars. Analogous to the one port case, we can define a model normalized reactance matrix $\xi_{ij} = X_{ij}/R_R$ for the case $R_R(k_n)$ constant for $n \leq N$ and $R_R(k_n) = 0$ for $n > N$,

$$\xi_{ij} = -\frac{1}{\pi} \sum_{n=1}^{N} \frac{w_{in} w_{jn}^*}{\tilde{k}^2 - \tilde{k}_n^2}, \tag{4.10}$$

where $\tilde{k}^2 = k^2/\Delta$, $w_{\ell n} = (w_{\ell n}^{(r)} + jw_{\ell n}^{(i)})/\sqrt{2}$, $w_{\ell n}^{(r)}$ and $w_{\ell n}^{(i)}$ are real, independent Gaussian random variables with zero mean and unit variance, $E(w_{in}^* w_{jn}) = \delta_{ij}$. Note that a unitary transformation, $\xi' = U\xi U^\dagger$, returns (4.10) with w_{in} and w_{jn} replaced by w_{in}' and w_{jn}' where $w_n' = Uw_n$. Since a unitary transformation does not change the covariance matrix, $E(w_{in} w_{jn}^*) = E(w_{in}' w_{jn}'^*) = \delta_{ij}$, the statistics of ξ and of ξ' are the same; i.e., their statistical properties are invariant to unitary transformations.

The universal fluctuation properties of the Z matrix can be described by the model matrix ξ_{ij} specified in Eq. (4.10). In the TRS case the w_{jn} are real Gaussian random variables with zero mean and unit width and the spacings satisfy Eq. (1.3). In the TRSB case the w_{jn} are complex and the spacings between adjacent k_n^2 satisfy Eq. (1.4).

4.2.1   Eigenvalue Correlations for the Impedance Matrix

In the case under consideration of multiple identical ports, ξ_{ij} will have a diagonal mean part $\bar{\xi}\delta_{ij}$ for which all the diagonal values are equal. The eigenfunctions of $\xi_{ij} = \bar{\xi}\delta_{ij} + \tilde{\xi}_{ij}$ and of its fluctuating part $\tilde{\xi}_{ij}$ will thus be the same. Consequently, we focus on the eigenvalues of the fluctuating part.

We initially restrict our considerations to the two-port case. We recall that for the lossless one-port case there is no difference in the statistics of the normalized impedance ξ for the TRS and TRSB cases. In both cases , it is Lorentzian with unit width. In the lossless two-port case, however, essential differences are observed when time reversal is broken. Using (4.10), we generate 10^6 realizations of the 2 by 2 matrix ξ in both the TRS and TRSB cases, again for $N = 2000$ and $k^2 = 1000$. In this test we generated spectra based on an independent spacings. For each realization we compute the eigenvalues of the ξ matrix. We find that in both the TRS and TRSB cases the eigenvalues of the ξ-matrix are Lorentzian distributed with unit width. That is, histograms of the eigenvalues generated according to the TRS and TRSB prescriptions are identical. However, if we consider the joint probability density function (PDF) of the two eigenvalues for each realization, then differences between the TRS and TRSB cases emerge. We map the two eigenvalues ξ_i, $i = 1$ or 2, into the range $[\pi/2, \pi/2]$ via the transformation $\theta_i = \arctan(\xi_i)$. Scatter plots of θ_2 and θ_1 for 10^6 random numerical realizations of the ξ matrix are shown in Fig. 4.1(a) for the TRS case and in Fig. 4.1(b) for the TRSB case. The white diagonal band in both cases shows that the eigenvalues avoid each other (i.e., they are anti-correlated). This avoidance is greater in the

TRSB case than in the TRS case. The correlation,

$$corr(\theta_1, \theta_2) \equiv \frac{\langle \theta_1 \theta_2 \rangle - \langle \theta_1 \rangle \langle \theta_2 \rangle}{\sqrt{\langle \theta_1^2 \rangle \langle \theta_2^2 \rangle}}, \tag{4.11}$$

is numerically determined to be -0.216 for the TRS case and -0.304 for the TRSB case.

From the construction of the ξ matrices for the TRS and TRSB cases their statistical properties are invariant under orthogonal and unitary transformations, respectively. Random matrix theory has been used to study these rotation-invariant ensembles and predicts the joint density function of θ_1 and θ_2 [46, 53] to be,

$$P_\beta(\theta_1, \theta_2) \propto |e^{j2\theta_1} - e^{j2\theta_2}|^\beta, \tag{4.12}$$

where $\beta = 1$ for the TRS case and $\beta = 2$ for the TRSB case. Note that based on Eq. (4.12), the probability density function for one of the angles $P(\theta_1) = \int d\theta_2 P(\theta_1, \theta_2)$ is uniform. From the definition $\theta = \arctan \xi$, this is equivalent to the eigenvalues of the ξ matrix having Lorentzian distributions.

The correlation coefficients calculated from the numerical results in Figs. 4.1(a) and 4.1(b) are consistent with the predictions of the random matrix theory from Eq. (4.12). This implies that the distribution of spacings and the long range correlations in the eigenvalues of the random matrix, which are ignored in the construction of the k_n^2 in the above computation are not important in describing the statistics of *lossless* impedance matrices. These correlations could be included using a sequence of k_n^2 generated by the eigenvalues of a random matrix. (We note that [54], lossy cavities yield statistics that are different in the TRS and TRSB cases.)

Now we test these predictions for numerical simulations of the chaotic cavity considered in the last chapter. We use the HFSS software to calculate the cavity

47
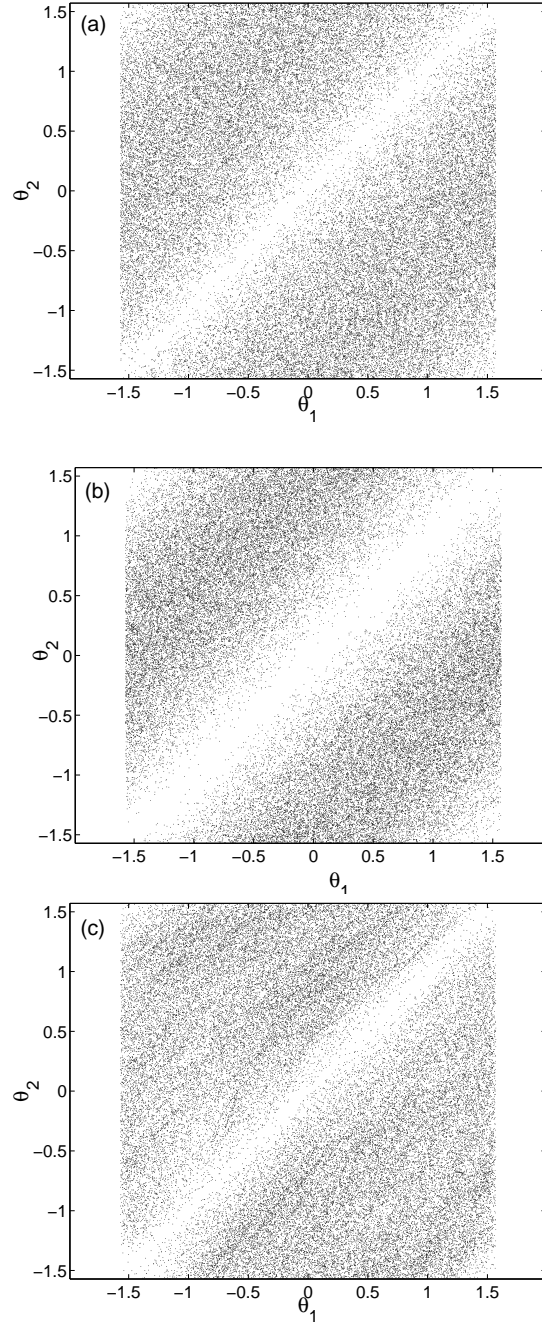
Figure 4.1: (a) Scatter plot of θ_1 vs θ_2, in the TRS case. (b) Scatter plot of θ_1 vs θ_2 in the TRSB case.(c) Scatter plot of θ_1 vs θ_2 from the HFSS simulation, with 100 realizations and sweeping frequency from 6.75GHz to 8.75GHz.

impedance matrix and radiation impedance matrix for a 2-port case. We locate the two ports, at the positions $(x, y)=(14\text{cm}, 7\text{cm})$ and $(x, y)=(27\text{cm}, 13.5\text{cm})$. We also include the 0.6 cm cylindrical perturbation which is located alternately at 100 random points in the cavity, and we numerically calculate the impedance matrix for 4000 frequencies in the range 6.75GHz to 8.75GHz. We obtain a normalized Z matrix, which is analogous to the ξ matrix defined in Eq. (4.10) according to

$$\xi_{hfss} = R_R^{-1}(Im[Z_{cav}] - 1_2 X_R),\qquad(4.13)$$

where 1_2 is the 2 by 2 identity matrix, Z_{cav} is the 2 by 2 impedance matrix calculated by HFSS, and X_R and R_R are the radiation reactance and resistance for a single port. For each realization of ξ_{hfss} we calculate its eigenvalues $\xi_i = \tan\theta_i$, $i = 1, 2$, and plot the values on the θ_1 vs. θ_2 plane, as shown in Fig. 4.1(c). The anti-correlation of the angles is seen in the figure, and $corr(\theta_1, \theta_2)$ from (4.11) is -0.205, which is comparable with what we expect for the TRS case, -0.216.

4.2.2 Independence of Eigenvalues and Eigenvectors of Z Matrix

So far we have focused on the eigenvalues of the impedance matrix. The eigenvectors of Z are best described in terms of the orthogonal matrix whose columns are the orthogonal eigenfunctions of Z. Specially, in the TRS case, since ξ is real and symmetric,

$$\xi = O \begin{pmatrix} \tan\theta_1 & 0 \\ 0 & \tan\theta_2 \end{pmatrix} O^T,\qquad(4.14)$$

where O^T is the transpose of O, and O is an orthogonal matrix, which we express in the form

$$O = \begin{pmatrix} \cos\eta & \sin\eta \\ -\sin\eta & \cos\eta \end{pmatrix}. \tag{4.15}$$

A scatter plot representing the joint pdf of the angle η and one of the eigenvalue angles θ_1 is shown in Fig. 4.2(a1). In analogy to how we obtain the realizations used in Fig. 3.1 in chapter 3, this plot is obtained by inserting random choices for the k_n^2 and w_{in} in (4.10). Notice that we have restricted η in Fig. 4.2(a1) to the range $0 \leq \eta \leq \pi/2$. This can be justified as follows. The columns of the matrix O in (4.15) are the eigenvectors of ξ. We can always define an eigenvector such that the diagonal components of O are real and positive. Further, since the eigenvectors are orthogonal, one of them will have a negative ratio for its two components. We pick this one to be the first column and hence this defines which of the two eigenvalues is θ_1. The scatter plots in Fig. 4.1 show that the restriction on η maintains the symmetry of θ_1 and θ_2, vis. $P_\beta(\theta_1, \theta_2) = P_\beta(\theta_2, \theta_1)$. Also in the Fig. 4.2(a2) (and (a3)), we plot the conditional distribution of θ (and η) for different values of η (and θ). As can be seen, these plots are consistent with η and θ being independent. This is also a feature of the random matrix model [22]. This independence will be exploited later when the S matrix is considered.

For TRSB systems, the ξ matrix is Hermitian $\xi^T = \xi^*$. A unitary matrix of eigenvectors that diagonalized it can be parameterized as

$$U = \begin{pmatrix} \cos\eta & \sin\eta\, e^{i\zeta} \\ -\sin\eta\, e^{-i\zeta} & \cos\eta \end{pmatrix} \tag{4.16}$$

Thus, there is an extra parameter ζ characterizing the complex eigenvectors of the ξ matrix. According to random matrix theory, the eigenfunctions and eigenvalues
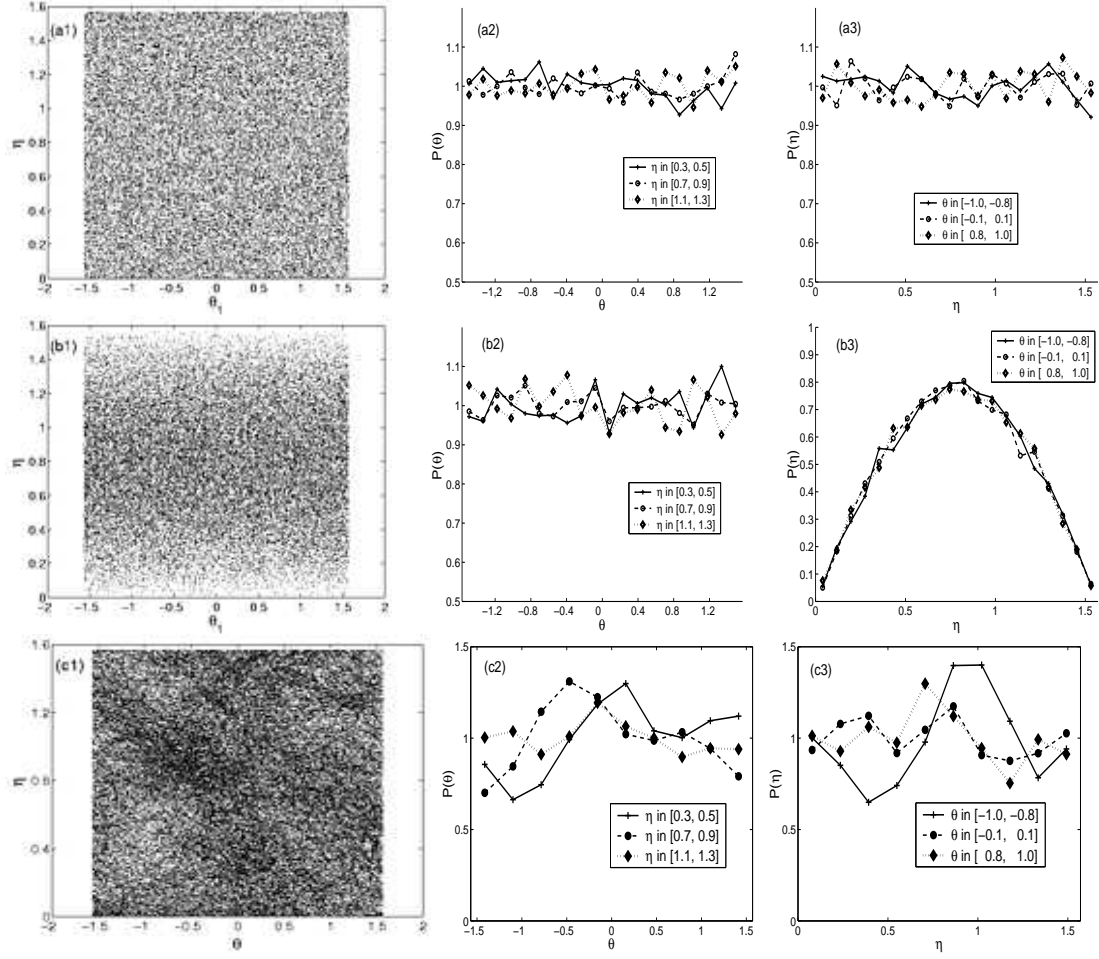
Figure 4.2: Scatter plot of η vs θ for (a1) the model impedance in the TRS case, (b1) the model impedance in the TRSB case, and (c1) from the HFSS simulation. Plots (a2) and (a3) [(b2) and (b3), (c2) and (c3)] show conditional probability for θ and for η for the model TRS case [model TRSB case, the HFSS simulation].

51

are independently distributed, i.e. η in the U matrix should be independent of θ_1, θ_2. This expectation is confirmed in Fig. 4.2(b) where a scatter plot of θ_1 vs η and conditional distributions of θ and of η are shown.

Again, we test the independence of θ and η with HFSS calculations. Using the ξ_{hfss} matrix obtained from Eq. (4.13), the angles θ and η can be recovered from the eigenvalues and the eigenvectors of the ξ_{hfss}. With the ensemble generated by sweeping the frequency from 6.75-8.75GHz and considering 100 different locations of our cylindrical perturbers, we obtain the joint distribution of θ and η in Fig. 4.2(c1) as well as their individual distributions in Fig. 4.2(c2) and (c3). Here we see that the distributions are qualitatively similar to those of the model impedance matrix in the TRS case. However, there are significant departures which need to be investigated. It is likely that these are the result of the same strong multi-path interference which gave rise to the reactance variations in the one port case shown in figure 3.2.

4.3   Effects of Distributed Loss

We now consider the effect of distributed losses in the cavity. By distributed losses, we mean losses that affect all modes in a frequency band almost equally. This is in contrast with the dissipation caused by the channels, which usually has significant modal fluctuations [62]. For example, wall losses and losses from a lossy dielectric that fills the cavity are considered distributed. For the case of losses due to conducting walls, the losses are approximately proportional to the surface resistivity, $\sim \sqrt{f}$, and vary little in a frequency range $\Delta f \ll f$. In addition, there will also be variation of wall losses from mode to mode due to different eigenmode structural details. These modal fluctuations, however, are

small when the modes are chaotic and the wavelength is short. We use the random coupling model to construct a complex cavity impedance accounting for distributed losses in a manner analogous to the lossless case, Eq. (2.22),

$$Z = -\frac{j}{\pi} \sum_n \Delta \frac{R_R(k_n)w_n^2}{k^2(1 - j\sigma) - k_n^2}, \qquad (4.17)$$

where σ represents the effect of losses. In particular, for loss due to wall absorption in a two-dimensional cavity, the value of σ is equal to the ratio of the skin depth of the conductor to the height of the cavity; if the cavity contains a lossy dielectric, σ is the loss tangent of the dielectric. The cavity quality factor is related to σ by $\sigma = Q^{-1}$, and Q is defined the same as $Q_{unloaded}$ in [62], i.e., we obtain the Q excluding the dissipation through the channels. This follows by noting that the real part of Z will have a Lorentzian dependence on frequency ($\omega = kc$) peaking at $\omega = k_nc$ with a full width at half maximum of $\omega\sigma$.

The impedance Z will have a real part and an imaginary part. We expect that, if $k^2\sigma \ll \Delta$, corresponding to small losses, then the real part will be zero and the imaginary part will have an approximately Lorentzian distribution. As losses increases such that $k^2\sigma \sim \Delta$ (the imaginary part of the denominators in (4.17) is of the order of eigenvalue spacing), the distributions of the real and imaginary part will change, reflecting that extremely large values of $|Z|$ are no longer likely. In the high loss limit, $k^2\sigma \gg \Delta$, many terms in the sum contribute to the value of Z. In this case, we expect Z will approach the radiation impedance with small (Gaussian) fluctuations.

In the Appendix C we evaluate the mean and variance of the real and imaginary part of the complex impedance (4.17) $Z = R + jX$. There it is shown that the mean is the radiation impedance $Z_R = R_R + jX_R$, and the variances of the real and imaginary parts are equal $Var[R] = Var[X]$. In general, the distribution

of R and X depends on the correlations between eigenvalues of k_n^2. However, in the low damping limit, the correlations are unimportant and we obtain

$$Var[R] = \frac{3R_R^2}{2\pi} \frac{\Delta}{k^2\sigma} \qquad (4.18)$$

for both the TRS and the TRSB cases. In the high damping limit $k^2\sigma \gg \Delta$, correlations are important and we obtain

$$Var[R] = \frac{R_R^2}{\pi} \frac{\Delta}{k^2\sigma} \qquad \text{for the TRS case}$$
$$Var[R] = \frac{R_R^2}{2\pi} \frac{\Delta}{k^2\sigma} \qquad \text{for the TRSB case.} \qquad (4.19)$$

This is to be contrasted with the result one would obtain if correlations in the eigenvalue spacing were neglected; i.e., if the k_n were assumed to be generated by adding independent spacings generated from the distributions (1.3) and (1.4). In that case, using the method in the Appendix C one obtains

$$Var[R] = \frac{R_R^2}{\pi} \frac{\Delta}{k^2\sigma} (\frac{1}{2} + \frac{2}{\pi}) \qquad \text{for the TRS case}$$
$$Var[R] = \frac{R_R^2}{\pi} \frac{\Delta}{k^2\sigma} (\frac{3\pi}{16}) \qquad \text{for the TRSB case.} \qquad (4.20)$$

These results are larger than those in Eq. (4.19) by 13.7% in the TRS case and 17.8% in the TRSB case, thus illustrating the necessity of generating the k_n^2 using random matrix theory if accurate results are desired in the lossy case $k^2\sigma > \Delta$.

In a recent experimental paper [57] the impedance statistics of a lossy TRS one-port microwave cavity were also considered. Their result is the same as (4.17). One difference is that they generate the realizations of k_n^2 solely by use of Eq. (1.3) with the assumption that the eigenvalue spacings are random independent variables.

We now investigate a model, normalized impedance, applicable in the one-port case with loss, which is the generalization of Eq. (3.5),

$$\zeta(\sigma) = -\frac{j}{\pi} \sum_{n=1}^{N} \frac{w_n^2}{\tilde{k}^2(1 - j\sigma) - \tilde{k}_n^2}. \qquad (4.21)$$

The normalized impedance ζ will have a real part $\rho > 0$ and an imaginary part ξ, $\zeta = \rho + j\xi$. We expect that if $\tilde{k}^2 \sigma \ll 1$, corresponding to small loss, then $\rho \cong 0$, and ξ will have an approximately Lorentzian distribution.

In analogy to Eq. (3.4) we write for the cavity impedance as Eq. (4.22)

$$Z = jX_R + R_R\zeta, \tag{4.22}$$

and we use (4.21) to generate probability distribution functions for the real and imaginary part of $\zeta = \rho + j\xi$. We first generate N values of w_n as independent Gaussian random variables of unit width (for this purpose we use a suitable random number generator). We next generate N values of the normalized eigenvalues $\tilde{k}_n^2$. To do this we have utilized two methods: (i) an approximate method based on Eq. (1.3) (for the TRS case) or Eq. (1.4) (for the TRSB case), and (ii) a method based on random matrix theory. We pick the value of k^2 relative to the spectrum k_n^2 such that the median of ξ is zero.

For method (i) we independently generate N values of s_n using the distribution (1.3) or (1.4). We then obtain $\tilde{k}_n^2$ as $\tilde{k}_n^2 = \sum_{n'=1}^{n} s_{n'}$. The main assumption of this method is that the spacings s_n can be usefully approximated as uncorrelated. On the other hand, it is known from random matrix theory that the spacings are correlated over long distance (in n), and the thus the assumption of method (i) is questionable (compare (46) and (47)). This motivates our implementation of method (ii) (See also [63]).

To implement method (ii) we generate an $M \times M$ random matrix with M large (M=1000) drawn from the appropriate ensemble (GOE or GUE) again using a random number generator. The width of the diagonal elements is taken to be unity. We then numerically determine the eigenvalues. The average spacing between eigenvalues of random matrices is not uniform. Rather, in the limit of
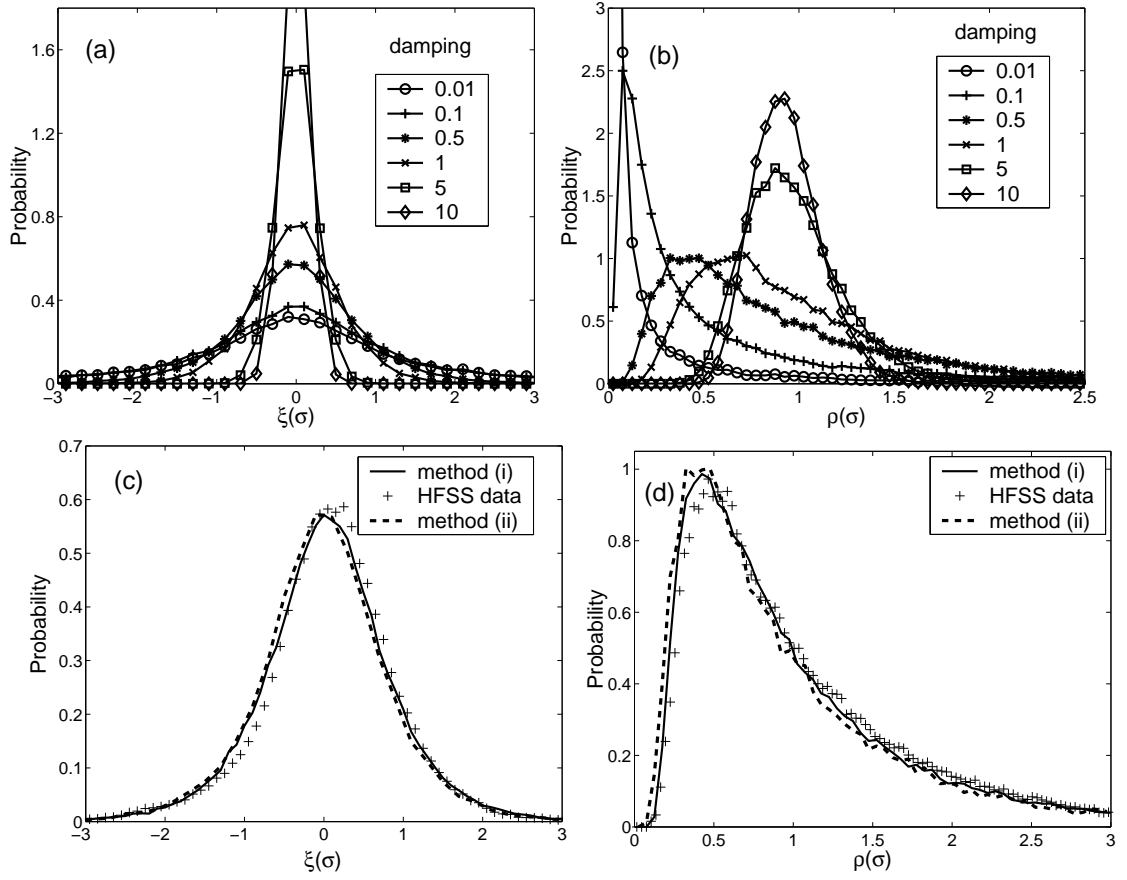
Figure 4.3: (a) Histogram of the imaginary part of $\zeta(\sigma)$ with different values of the damping obtained with method (ii); (b) Histogram of the real part of $\zeta(\sigma)$ with different damping obtained with method (ii). (c) and (d) are histograms of the reactance and resistance from HFSS calculation with a lossy top and bottom plate, compared with histograms from Eq. (4.21) computed as in (a) and (b) (dashed line) and by method (i) (solid line).

large M, the eigenvalues λ are distributed in the range $-\sqrt{2M} < \lambda < \sqrt{2M}$, and the average spacing for eigenvalues near an eigenvalue λ is given by

$$\Delta(\lambda) = \pi/\sqrt{2M - \lambda^2} \qquad (4.23)$$

in both the TRS and TRSB cases. In order to generate a sequence of eigenvalues with approximately uniform spacing we select out the middle 200 levels. We then normalize the eigenvalues by multiplying $1/\Delta(0)$ to create a sequence of $\tilde{k}_n^2$ values with average spacing of unity.

Histogram approximations to the GOE probability distributions of $Re[\zeta]$ and $Im[\zeta]$ obtained by use of (4.21) and method (ii) are shown in Figs. 7(a) and 7(b). These were obtained using 30,000 random GOE matrix realizations of 1000 by 1000 matrices and selecting the middle 200 eigenvalues of each realization. The resulting graphs are shown for a range of damping values, $\tilde{k}^2\sigma$=0.01, 0.1, 0.5, 1, 5 and 10. As seen in Fig. 4.3(a), when $\tilde{k}^2\sigma$ is increased, the distribution of ξ values becomes "squeezed". Namely, the Lorentzian tail disappears and the fluctuations in ξ decrease. Eventually, when σ enters the regime, $1 \ll \tilde{k}^2\sigma \ll N$, the probability distribution function of $\xi(\sigma)$ approaches a narrow Gaussian distribution centered at $\xi = 0$ (recall that $\bar{\xi} = 0$). As shown in Fig. 4.3(b), as σ increases from zero, the distribution of the real part of $\zeta(\sigma)$ which, for $\sigma = 0$, is a delta function at zero, expands and shifts toward 1, becoming peaked around 1. In the very high damping case, both the real part and imaginary parts of ζ, ρ and ξ, will be Gaussian distributed with the mean value equal to 1 and 0 respectively, and the same variance inversely proportional to the loss (as shown in the Appendix C). As a consequence, the reflection coefficient $|S|^2$ in the high damping limit, is exponentially distributed. This result is consistent with the theoretical discussion given by [63].

In general, the complex impedance distribution is not described using simple distributions such as Gaussian or Lorentzian. The distribution of the real part of the impedance has been studied in connection with the theory of mesoscopic systems and known as the "local density of states"(LDOS). Through the supersymmetry approach, Efetov obtained the probability density function for the LDOS in systems without time reversal symmetry[65]. For chaotic systems with time reversal symmetry, the corresponding exact formula was derived in the form of a multiple integral [66]. However the difficulty to carry out the five-fold integral makes it hard to interpret the formulas in Ref. [66]. Very recently, Fyodorov and Savin have proposed interpolation formulas for the impedance distributions at arbitrary values of damping parameter [67]. The suggested formulas satisfy all the asymptotic behaviors in the physically interesting limiting cases, e.g. weak damping or very strong damping cases. Furthermore, these formulas seem to agree pretty well with the results of the numerical simulations, though the agreement in the intermediate damping case is not as good as in the limiting cases. Here we still use the histograms generated from the Monte-Carlo simulations as a comparison to the HFSS data, however, we believe the formula presented by Fyodorov and Savin would be very helpful for most practical purposes of comparison.

Using HFSS, we simulate the lossy case by specifying the material on the top and bottom plates to be an imperfect conductor with a bulk resistivity of 70 $m\Omega \cdot cm$. In this case we can calculate a value of $\sigma = \delta/h = 0.002$, where δ is the skin depth at frequency of 7.75GHz (at the middle of the sweeping range) and $h = 0.2cm$ is the cavity height in the numerical simulation. The corresponding parameter $\tilde{k}^2 \sigma$ is 0.5 at 7.75GHz. Histogram results for the normalized reactance

(ξ) and resistance (ρ) fluctuations of $\zeta_{hfss} = R_R^{-1}(Z_{cav} - jX_R) = \rho + j\xi$ are plotted in Figs. 4.3(c) and 4.3(d) together with the histograms generated from Eq. (4.21), and using spectra from the random matrices. As can be seen, the histograms from the HFSS simulations match those of the model.

Chapter 5

Statistics of the Scattering Matrix

5.1   Introduction

The universal distribution of chaotic scattering matrices can be described by Dyson's circular ensemble [22, 53]. However, the circular ensemble cannot be directly compared with experimental data because it applies only in the case of 'ideal coupling' (which we define subsequently), while in experiments there are there are non-ideal, system-specific effects due to the particular means of coupling between the scattering system (e.g, a microwave cavity) and the outside world. This non-universality of the raw experimental scattering data has long been appreciated and addressed in theoretical work [49, 58, 59]. Of particular note is the work of Mello, Peveyra and Seligman (MPS) which introduces the distribution known as the Poisson kernel, where a mean scattering matrix $\langle S \rangle$ is used to parameterize the non-ideal coupling. To apply this theory to a practical case it is typically necessary to specify a procedure for determining a measured estimate of $\langle S \rangle$ [60, 61], which usually is through an averaging over a number of configurations and over a suitable frequency range.

Note that the quantity $\langle S \rangle$ in the MPS theory describes direct(or prompt)

process [49, 63] that depend only on the local geometry of the coupling ports, as opposed to complicated chaotic processes resulting from multiple reflections far removed from the coupling port. Thus in principle, a non-statistical quantity could be expected to characterize the coupling. In this chapter I pursue another approach. Specifically we seek to characterize the coupling in a manner that is both independent of the chaotic system and obtainable without employing averages. As discussed in the previous two chapters, a direct approach can be based on the determination of the radiation impedance of the port Z_R or equivalent S_R, the complex radiation scattering matrix, which describes prompt process at the port and can be shown to be equal to $\langle S \rangle$. The perfect coupling case corresponds to $S_R = 0$, in which all incident wave energy enters the cavity.

5.2 Reflection Coefficient in the One Port Case

5.2.1 One Port Lossless Case

In Chapter 3, we obtained a universal Lorentzian distribution for the chaotic cavity impedance Z, after normalization by the radiation impedance, $Z = j(X_R + R_R \xi)$, where ξ is a zero mean, unit width Lorentzian random variable. We now consider the consequences for the reflection coefficient. Suppose we can realize the perfect coupling condition, i.e. $R_R = Z_0$, $X_R = 0$, in which the wave does not "feel" the transition from the cable to the cavity. In this case the cavity reflection coefficient becomes

$$S = \frac{j\xi - 1}{j\xi + 1} = \exp[-j(2\tan^{-1}\xi + \pi)]. \tag{5.1}$$

A standard Lorentzian distribution for ξ corresponds to a uniform distribution for $\tan^{-1}\xi$ from $[-\pi/2, \pi/2]$, and thus to a reflection coefficient uniformly distributed

on the unit circle.

In the general case (i.e., non-perfect coupling), we introduce $\gamma_R = R_R/Z_0$, $\gamma_X = X_R/Z_0$, and express S as

$$S = e^{j\phi} = (Z + Z_0)^{-1}(Z - Z_0) = \frac{j(\gamma_R \xi + \gamma_X) - 1}{j(\gamma_R \xi + \gamma_X) + 1}. \tag{5.2}$$

We replace the Lorentzian random variable ξ by introducing another random variable ψ via $\xi = \tan(\psi/2)$. Using this substitution, the Lorentzian distribution of ξ translates to a distribution of ψ that is uniform in $[0, \, 2\pi]$. We then have from Eq. (5.2)

$$e^{j(\phi - \phi_R)} = \frac{e^{-j\psi'} + |\rho_R|}{1 + |\rho_R|e^{-j\psi'}}, \tag{5.3}$$

where the "free space reflection coefficient" ρ_R

$$\rho_R = |\rho_R|e^{j\phi_R} = \frac{\gamma_R + j\gamma_X - 1}{\gamma_R + j\gamma_X + 1}, \tag{5.4}$$

is the complex reflection coefficient in the case in which the cavity impedance is set equal to the radiation impedance ($\tilde{\xi} = -j$), and $\psi' = \psi + \pi + \phi_R + 2\tan^{-1}[\gamma_X/(\gamma_R + 1)]$ is a shifted version of ψ. Equations for the magnitude and phase of the free space reflection coefficient ρ_R can be obtained from Eq. (5.4). Specifically,

$$|\rho_R| = \sqrt{\frac{(\gamma_R - 1)^2 + \gamma_X^2}{(\gamma_R + 1)^2 + \gamma_X^2}}, \tag{5.5}$$

and

$$\tan \phi_R = \frac{2\gamma_X}{\gamma_R^2 + \gamma_X^2 - 1}. \tag{5.6}$$

Eq. (5.3) is essentially a statement of the Poisson kernel relation for a non-perfectly coupled one port cavity.

To compute the probability distribution function for ϕ, $P_\phi(\phi)$, we note that, since ψ is uniformly distributed on any interval of 2π, we can just as well take

62

ψ', which differs from ψ by a constant shift, to be uniformly distributed. Consequently, we have

$$P_\phi(\phi) = \frac{1}{2\pi} \left| \frac{d\psi'}{d\phi} \right|$$
$$= \frac{1}{2\pi} \frac{1 - |\rho_R|^2}{1 + |\rho_R|^2 - 2|\rho_R| \cos(\phi - \phi_R)}. \tag{5.7}$$

Thus $P_\phi(\phi)$ is peaked at the angle ϕ_R corresponding to the phase angle of the free space reflection coefficient, with a degree of peaking that depends on $|\rho_R|$, the magnitude of the free space reflection coefficient. 'Perfect matching' corresponds to $\gamma_R = 1$, $\gamma_X = 0$, and $|\rho_R| = 0$, in which case $P_\phi(\phi)$ is uniform.

We next consider the case of poor matching for which $|\rho_R| \cong 1$ and $P_\phi(\phi)$ is strongly peaked at ϕ_R. This behavior can be understood in the context of the frequency dependence of the phase for a given realization. It follows from (5.2) and (3.5) that the phase ϕ decreases by 2π as k^2 increases by the spacing between eigenvalues. If $|\rho_R| \cong 1$, then for most of the frequencies in this interval, the phase is near ϕ_R. However, for the small range of frequencies near a resonance, the phase will jump by 2π as the resonance is passed. This indicates that the mode of the cavity is poorly coupled to the transmission line. In the case of good matching, $|\rho_R| = 0$, all phases are equally likely indicating that, as a function of frequency, the rate of increase of phase is roughly constant. This implies that the resonances are broad, and the cavity is well coupled to the transmission line.

In order to describe the different coupling strengths, we consider the parameter g originally introduced by Fyodorov and Sommers [46] :

$$g = \frac{1 + |\langle e^{j\phi} \rangle|^2}{1 - |\langle e^{j\phi} \rangle|^2}. \tag{5.8}$$

Evaluating $\langle S \rangle$ using Eq. (5.7),

$$g = \frac{1 + |\rho_R|^2}{1 - |\rho_R|^2}. \tag{5.9}$$
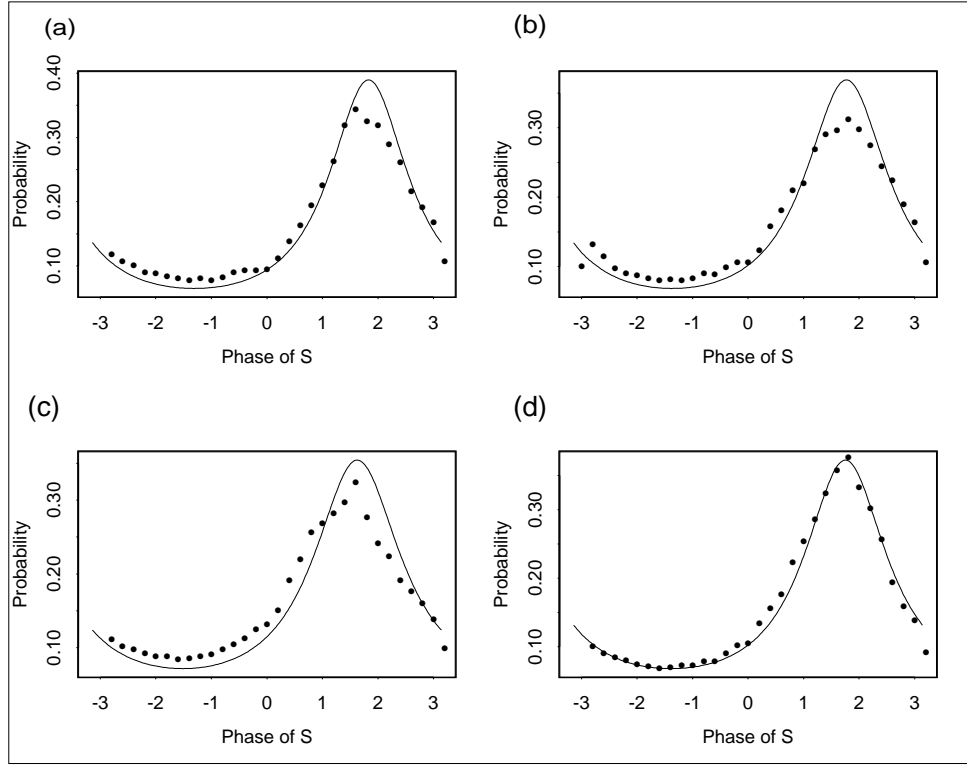
Figure 5.1: Histogram of the reflection phase distribution for an HFSS calculation for the cavity in Fig. 2.1 with center frequencies located at (a) 7GHz, (b) 7.5GHz, (c) 8GHz, (d) 8.5GHz, and with sweeping span equal to 0.1GHz. Numerical data are compared with Eq. (5.7) using parameters determined by Z_R at the corresponding center frequencies.

Thus, g has a minimum value of 1 in the perfectly matched case and is large if the matching is poor, $|\rho_R| \sim 1$. An analogous quantity is the voltage standing wave ratio on the transmission line when the cavity impedance is set equal to the radiation impedance,

$$\text{VSWR} = \frac{1 + |\rho_R|}{1 - |\rho_R|} = g + \sqrt{g^2 - 1}. \tag{5.10}$$

To test Eq. (5.7), we compared its predictions for the phase distribution with direct numerical calculations obtained using HFSS (High Frequency Structure

64

Simulator) for the case of the cavity and coupling detail as specified in Fig. 3.3. As compared to what was done for Fig. 3.3, we have narrowed the frequency range to 0.1 GHz bands for each realization in 1000 10^{-4} GHz steps centered at 7 GHz, 7.5 GHz, 8 GHz, 8.5 GHz. Instead of calculating the radiation impedance for every frequency, we use the value of Z_R at the middle frequency of the interval in calculating the values of γ_R and γ_X. We present theoretical phase density distribution functions together with numerical histogram results in Fig. 5.1. The agreement between the theory, Eq. (5.7), and the numerical results is surprisingly good, especially considering the rather small (0.1GHz) frequency range used.

5.2.2 One Port Lossy Case

In Chapter 4 we noted that the variance of the real and imaginary parts of the complex impedance are equal. There is a more fundamental connection between these that is revealed by considering the reflection coefficient in the perfectly matched case,

$$\alpha e^{j\phi} = (\zeta - 1)/(\zeta + 1), \tag{5.11}$$

where α and ϕ are random variables giving the magnitude and phase of the reflection coefficient. It can be argued [63] that ϕ and α are independent and that ϕ is uniformly distributed in $[0, 2\pi]$, which is similar to the independence to eigenvalues and eigenvectors of impedance matrices. The magnitude α is distributed on the interval $[0, 1]$ with a density that depends on losses. A plot of the probability distribution for α taken from the data in Figs (4.3a) and (4.3b) is shown in Fig 5.2, for the damping values 0.1, 0.5, 1 and 5. Recently, experimental findings for the statistical properties of the normalized scattering coefficient (corresponding to the reflection coefficient in the perfect coupling case) has been reported
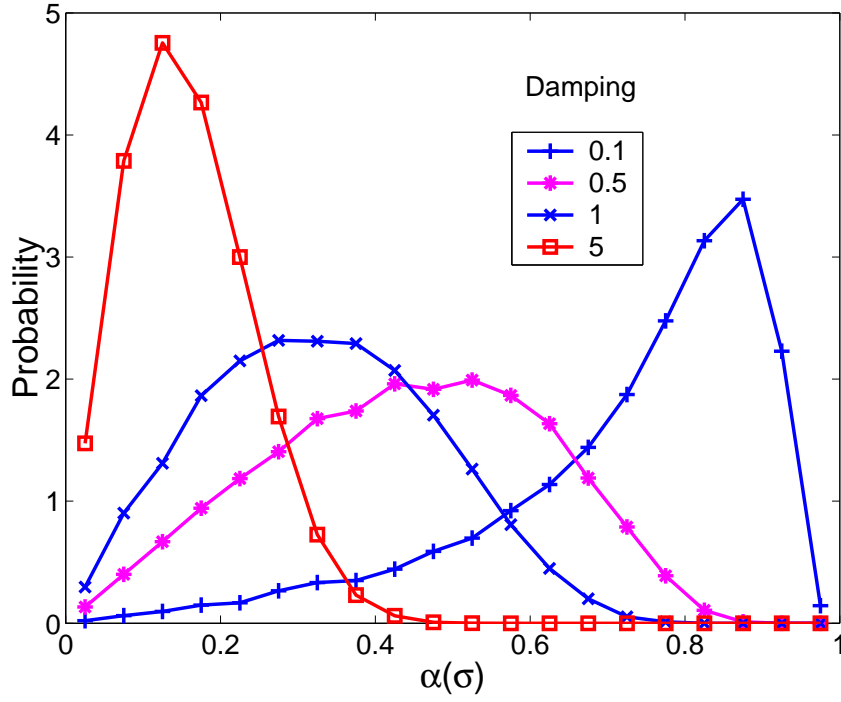
Figure 5.2: Histogram of the magnitude of reflection coefficient in the Eq. (5.11), $\alpha(\sigma)$, with different values of the damping.

by Hemmady et al.[64]. For different coupling geometries and and degrees of loss, the experimental data strongly support the hypothesis that the magnitude α is statistically independent of the phase ϕ, and that the phase ϕ is uniformly distributed in 0 to 2π.

We can express the actual complex reflection coefficient ρ in terms of the normalized reflection coefficient by first finding the normalized impedance from (5.11), $\zeta = (1 + \alpha e^{j\phi})/(1 - \alpha e^{j\phi})$ calculating the cavity impedance from (4.22), and expressing the result in terms of the radiation reflection coefficient (5.4). The result is

$$\rho = \frac{\rho_R + \alpha e^{j(\phi + \Delta\phi)}}{1 + \alpha e^{j(\phi + \Delta\phi)}\rho_R^*}, \tag{5.12}$$

where $\tan(\Delta\phi/2) = -X_R/(R_R + Z_0)$ depends on system specific parameters. Since the angle ϕ is uniformly distributed, it can be shifted by $\Delta\phi$ thus eliminating $\Delta\phi$ from the expression. Eq. (5.12) is then a restatement of the Poisson kernel in the single port case.

The independence of α and ϕ in Eq. (5.11) also guarantees the invariance of the distribution of cavity impedances when a lossless two port is added as in section 3.4. In particular, the normalized cavity impedance ζ before the addition of the two port is given by

$$\zeta = \frac{Z - jX_R}{R_R} = \frac{1 + \alpha e^{j\phi}}{1 - \alpha e^{j\phi}}. \tag{5.13}$$

With the addition of the lossless two port as shown in the Fig. 3.4, impedances are transformed to Z', X'_R, and R'_R such that

$$\zeta = \frac{Z' - jX'_R}{R'_R} = \frac{1 + \alpha e^{j(\phi - \phi_c)}}{1 - \alpha e^{j(\phi - \phi_c)}}. \tag{5.14}$$

where $\phi_c = (2\beta + \pi)$ depends only on the properties of the two port and the cavity coupling port and the angle β satisfies

$$\begin{aligned}
\cos\beta &= \frac{R_R}{\sqrt{R_R^2 + (X_{11} + X_R)^2}}, \\
\sin\beta &= \frac{(X_{11} + X_R)}{\sqrt{R_R^2 + (X_{11} + X_R)^2}}.
\end{aligned} \tag{5.15}$$

Since ϕ is uniformly distributed, so is the difference $\phi - \phi_c$. Consequently, the normalized random variables ζ and ζ' have identical statistical properties.

A by-product of (5.13) is that we can easily prove that its real part $\rho = (1-\alpha^2)/(1+\alpha^2-2\alpha\cos\phi)$ and its imaginary part $\xi = (2\alpha\sin\phi)/(1+\alpha^2-2\alpha\cos\phi)$ have the same variance and zero correlation. Since α and ϕ are independent, we can carry out the integration over the uniformly distributed ϕ and obtain

$$Var[\rho] = Var[\xi] = \langle\frac{1 + \alpha^2}{1 - \alpha^2}\rangle_\alpha - 1, \qquad Cov[\rho, \xi] = 0 \tag{5.16}$$

where $\langle .. \rangle_\alpha$ denotes average over α. This property has been tested in microwave cavity experiments with excellent agreements [16]. For the high damping case, $\rho - 1$ and ξ will become two independent Gaussian variables with zero mean and small but same variances. This yields an exponential distribution for the α^2, which is consistent with the result obtained by Kogan [63] based on the "maximum information entropy" principle. For the weakly absorptive case, Beenakker and Brouwer [68] studied the distribution of α^2 in the TRSB case through the time-delay matrix and obtained a generalized Laguerre ensemble. However, for a TRS system with arbitrary loss, there is no simple formula for the distribution of reflection coefficients.

We noted from Eq. (5.13) that ζ^{-1} and ζ have the same distribution because the phase ϕ is uniformly distributed and independent of the amplitude α.(The quantity ζ^{-1} may be regarded as the normalized admittance.) This prediction for ζ^{-1} was stimulated by a private communication with D. V. Savin and it agrees with experimental data.

5.3   Reflection Coefficient in the Multiport Case

In this section, we use our knowledge of the statistical properties of the Z matrix to deduce properties of the S matrix, particularly for the ensemble average of the reflection coefficient $\langle |S_{11}|^2 \rangle$. For a system with two ports, in the lossless case considered here we note $\langle |S_{12}|^2 \rangle = 1 - \langle |S_{11}|^2 \rangle$

According to the previous section, for the case of non-perfect coupling, model of the cavity impedance matrix can be expressed as $Z = \hat{R}_R^{1/2} \xi \hat{R}_R^{1/2} + j\hat{X}_R$, where Z_R is the 2×2 radiation impedance and ξ is a 2×2 random matrix generated according to Eq. (4.10). If the incoming frequency is restricted in a narrow

range, the radiation impedance Z_R is essentially constant. In this section we assume that identical ports are connected to identical transmission line, i.e., Z_R and the transmission line characteristic impedance Z_0 are diagonal matrices with equal diagonal elements. Thus, we obtain the expression for the S matrix, $S = (Z + Z_0)^{-1}(Z - Z_0)$,

$$S = [(\gamma_R \xi + j\gamma_X 1_2) + 1_2]^{-1}[(\gamma_R \xi + j\gamma_X 1_2) - 1_2], \tag{5.17}$$

where $\gamma_R = R_R/Z_0$, $\gamma_X = X_R/Z_0$ are scalars and 1_2 is the 2×2 identity matrix . The two parameters γ_R and γ_X, as we show later, fully specify the coupling effects on the wave transport process. The special case of perfect coupling corresponds to $\gamma_R = 1$ and $\gamma_X = 0$.

5.3.1   Lossless Two-port Case

We recall that for TRS systems the reactance matrix X is real and symmetric, and can be diagonalized by an orthogonal matrix O, Eq. (4.15). If identical ports are connected to identical transmission lines of characteristic impedance Z_0, then the scattering matrix S is also diagonalized by O, and we can write

$$S = O \begin{pmatrix} e^{j\phi_1} & 0 \\ 0 & e^{j\phi_2} \end{pmatrix} O^T. \tag{5.18}$$

The scattering phases ϕ_1 and ϕ_2 are then related to the eigenvalue angles θ_i by formulas analogous to the one-port case, $\tan(\pi/2 - \phi_i/2) = \gamma_R \tan\theta_i + \gamma_X$.

Substituting Eq. (4.15) for O in (5.18) and multiplying the matrices, we obtain

$$|S_{11}|^2 = \cos^4\eta + \sin^4\eta + 2\cos^2\eta \sin^2\eta \cos(\phi_1 - \phi_2). \tag{5.19}$$

We can now compute the expected value of the square of $|S_{11}|$ by assuming that η is independent of the angles ϕ_1 and ϕ_2 and is uniformly distributed, which yields

$\langle\cos^4\eta + \sin^4\eta\rangle = 3/4$, $2\langle\cos^2\eta\sin^2\eta\rangle = 1/4$ and

$$\langle|S_{11}|^2\rangle = \frac{3}{4} + \frac{1}{4}\langle\cos(\phi_1 - \phi_2)\rangle. \tag{5.20}$$

Assuming the angles θ_1 and θ_2 are distributed according to Eq. (4.12) and using the relation between $\phi_{1,2}$ and $\theta_{1,2}$, evaluation of $\langle\cos(\phi_1 - \phi_2)\rangle$ is carried out in Appendix D. The result is

$$\langle|S_{11}|^2\rangle = 1 - \frac{1 - |\rho_R|^4}{8|\rho_R|^2} - \frac{(1 - |\rho_R|^2)^3}{16|\rho_R|^3}\ln\frac{1 - |\rho_R|}{1 + |\rho_R|}, \tag{5.21}$$

where the "the free space reflection coefficient" ρ_R is defined as the same way in the last section.

We first check the asymptotic behavior for the power transmission coefficient $T = 1 - |S_{11}|^2$ implied by the formula (5.21). In the non-coupled case, $|\rho_R| = 1$, i.e., all the incoming power is reflected, and we obtain from (5.21) $\langle T\rangle = 0$. On the other hand, in the perfect coupling case, $|\rho_R| = 0$, $\ln[(1 + |\rho_R|)/(1 - |\rho_R|)]$ in the (5.21) can be expanded as $2(|\rho_R| - |\rho_R|^3/3)$. Therefore, $\langle T\rangle = 1/3$. This is consistent with the result in Ref. [63], $\langle R\rangle = 2\langle T\rangle$. That is, in the perfect coupling case the average of the reflected power is twice that of the transmitted.

Eq. (5.21) shows that the averaged power reflection and transmission coefficients only depend on the magnitude of ρ_R and not its phase. A plot of $\langle|S_{11}|^2\rangle$ versus $|\rho_R|$ is shown in Fig. 5.3(a). Also shown are data points obtained by taking 10^6 realizations of the impedance matrix (4.10) with eigenvalue statistics generated from TRS spectrum and computing the average of $|S_{11}|^2$ for different combinations of γ_R and γ_X characterizing the radiation impedance. The data confirm that the average of $|S_{11}|^2$ depends only on the magnitude of the free space reflection coefficient and not its phase.

In the TRSB case, the eigenvalues of the X matrix are still real, but the

70

eigenvectors are complex. In this case, Eq. (5.18) is replaced by

$$S = U \begin{pmatrix} e^{j\phi_1} & 0 \\ 0 & e^{j\phi_2} \end{pmatrix} U^\dagger, \tag{5.22}$$

where the unitary matrix U is given by Eq. (4.16). Multiplying the matrices in Eq. (5.22), we find the same expression for $|S_{11}|^2$, Eq. (5.19), as in the TRS case. The average of $|S_{11}|^2$ will be different in the TRSB case because of the different statistics for η, θ_1 and θ_2 which characterize the eigenfunctions and eigenvalues of the impedance matrix. In particular, η has a distribution, arising from the SU(2) group [70],

$$P_\eta(\eta) = |\sin(2\eta)|, \tag{5.23}$$

which yields $\langle \cos^4 \eta + \sin^4 \eta \rangle = 2/3$, $2\langle \cos^2 \eta \sin^2 \eta \rangle = 1/3$, thus,

$$\langle |S_{11}|^2 \rangle = \frac{2}{3} + \frac{1}{3} \langle \cos(\phi_1 - \phi_2) \rangle. \tag{5.24}$$

Recalling that θ_1 and θ_2 are distributed according to (4.12) with $\beta = 2$, this results in a different set of integrals (see Appendix D). The result is

$$\langle |S_{11}|^2 \rangle = 1 - \frac{(|\rho_R|^2 - 1)(|\rho_R|^2 - 3)}{6}, \tag{5.25}$$

which depends only on the magnitude of the free space reflection coefficient. A plot of $\langle |S_{11}|^2 \rangle$ from Eq. (5.25) versus $|\rho_R|$ is also shown in Fig. 5.3(a), along with data point obtained by taking 10^6 realizations of the TRSB impedance matrix (4.10) generating from random numbers and computing the average of $|S_{11}|^2$ for different combinations of γ_R and γ_X characterizing the free space impedance. Once again, the data collapse to the curve predicted in Eq. (5.25).

We now test the relation between $\langle |S_{11}|^2 \rangle$ and $|\rho_R|$ with the impedance matrices we obtained from the HFSS two-port calculations. We can vary the transmission line impedance Z_0 and generate $\langle |S_{11}|^2 \rangle$ and $|\rho_R|$. However, the range of
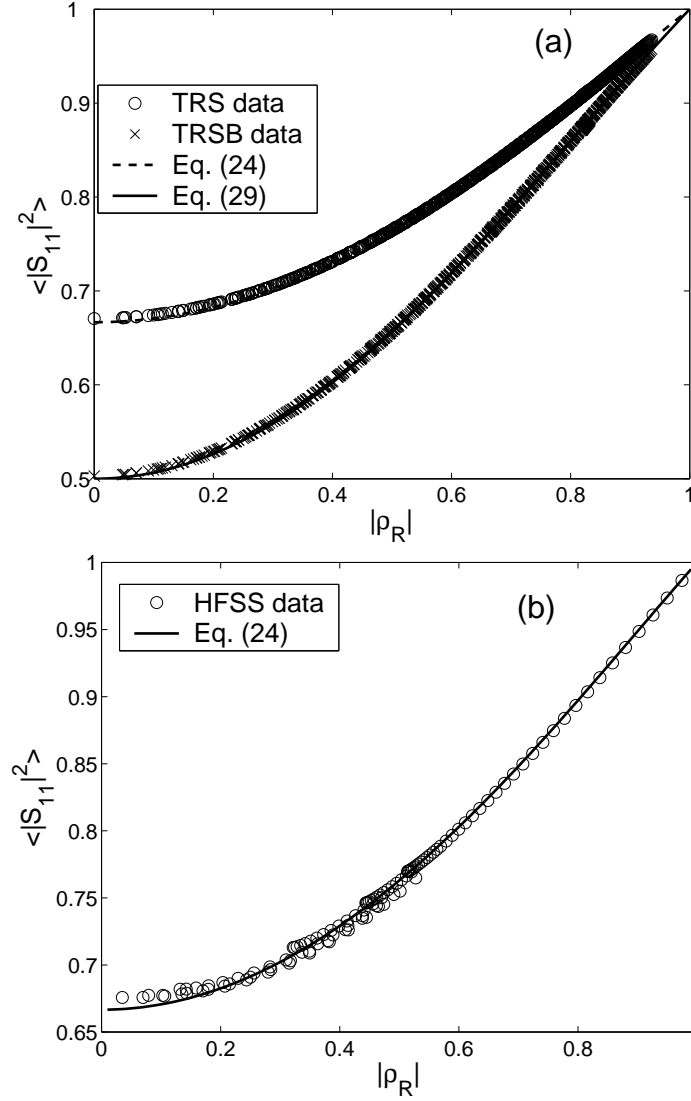
Figure 5.3: (a) Numerical simulation for the average reflection coefficient $\langle |S_{11}|^2 \rangle$ vs magnitude of ρ_R defined in Eq. (5.4) for the TRS and the TRSB system, taking 10^6 realization of the impedance matrix, 30 uniformly spaced values of γ_R from 0.1 to 3, and 31 equally spaced values of γ_X from 0 to 3. (b) Average reflection coefficient $\langle |S_{11}|^2 \rangle$ vs $|\rho_R|$ using the cavity impedance and radiation impedance from HFSS calculation and varying the values of Z_0 and the capacitive reactance Y

$|\rho_R|$ values accessible doing this is limited because of the large inductive radiation reactance associated with the coupling port. To extend the range of $|\rho_R|$ we add a shunt susceptance $Y = (j\omega C)$ in parallel with each port. This results in a modified cavity impedance matrix $Z'_{cav} = (Z_{cav}^{-1} + j\omega C 1_2)^{-1}$. We then form the scattering matrix

$$S = (Z'_{cav} + Z_0)^{-1}(Z'_{cav} - Z_0). \tag{5.26}$$

The corresponding free space reflection coefficient is generated by $Z'_R = (Z_R^{-1} + j\omega C)^{-1}$ and $|\rho_R| = |Z'_R + Z_0|^{-1}|Z'_R - Z_0|$. By choosing appropriate combinations of ωC and Z_0, we can achieve a range of $|\rho_R|$ values between 0 and 1. For each $|\rho_R|$ value, we average $|S_{11}|^2$ over frequencies and realizations and plot the points on Fig. 5.3(b). These compare favorably with the theoretical result (solid curve) based on the random matrix theory results.

5.3.2   M-port Case, $M > 2$

Using the random coupling model (4.10) and assuming perfect coupling $\gamma_R = 1$, $\gamma_X = 0$ (i.e. $|\rho_R| = 0$), we have simulated the S matrix for cases of two to seven, 13 and 57 ports. The results for the average reflection and transmission coefficients were found to satisfy:

$$\text{TRS}: \qquad \langle |S_{ij}|^2 \rangle = \begin{cases} \frac{2}{M+1} & i = j, \\ \frac{1}{M+1} & i \neq j, \end{cases} \tag{5.27}$$

and

$$\text{TRSB}: \qquad \langle |S_{ij}|^2 \rangle = \begin{cases} \frac{1}{M} & i = j, \\ \frac{1}{M} & i \neq j, \end{cases} \tag{5.28}$$

where M is the number of ports connecting the cavity to transmission lines. It seems that, in the TRS case, the input waves "remember" their entry port and

have a preference for reflection through it (this is related to the concept of "weak localization" reviewed in [71]). In contrast, for the TRSB case, the waves behave as if they forget through which port they entered the cavity, and thus all the ports have equal probability of being the output for the waves.

It was shown by Brouwer and Beenakker [14] that scattering in multiport lossless systems can be related to that in a single-port, lossy system. It was proposed that the introduction of N' ($N' \gg 1$) fictitious ports of a lossless system would give equivalent statistics for the reflection coefficient as would be obtained for a single port model with a uniform internal loss. Considering a system with M ports all perfectly matched, we can pick port 1 as the input and consider the other ports as a form of dissipation. Due to the energy escaping from the other $(M-1)$ ports, we will obtain a reflection coefficient S_{11} with magnitude less than one, which is similar to that obtained in the one-port lossy case (i.e., with losses due to finite wall conductivity). The cavity impedance seen from port 1, Z_1, is calculated from S_{11}, one of the elements from the M by M scattering matrix,

$$Z_1 = R_R \frac{1 + S_{11}}{1 - S_{11}} + jX_R. \tag{5.29}$$

When normalized by the radiation impedance this corresponds to a complex impedance $\zeta_M = (1 + S_{11})/(1 - S_{11}) = \rho + j\xi$. On the other hand, we can generate the lossy one-port impedance ζ from Eq. (4.17), modelling the lossy effect by adding a small imaginary term to the frequency [13]. We can then compare the statistics of ζ from the lossy one port and ζ_M from the M-port lossless case (We note that approximate analytic formula for the distributions of the real and imaginary parts of ζ have recently been given by Fyodorov and Savin [67]). An appropriate value of the damping parameter in the one port case, $\tilde{k}^2\sigma$

($\sigma = 1/Q$), can be determined so that the average value of $|S_{11}|^2$ in the lossy case is equal to $2/(M+1)$ for the TRS case (or $1/M$ for the TRSB case). Then we can compare the real and imaginary parts of the impedances obtained in the two different ways. In Fig. 5.4, we include the results for the three different number of ports, M=4, 13 and 57, and the corresponding one port result. For $M = 4$ we note that the distributions are similar but clearly not the same. However, for M=13 or 57, the distributions for ζ and ζ_M are much closer. Thus, we confirm that distributed damping and a large number of output channels are equivalent so as to affect the distribution of the sub-unitary scattering matrix.

We now briefly discuss the multiport case with $M > 2$ and with mismatch ($|\rho_R| > 0$). As long as the assumption that the eigenfunctions (η) and the eigenvalues (θ or ϕ) are independent is still true, $\langle |S_{11}|^2 \rangle$ is related to the mismatch only through $\langle \cos(\phi_k - \phi_l) \rangle$, similar to the expression in Eq. (5.20). The same series of steps specified in the Appendix D can be carried out to show that $\langle \cos(\phi_k - \phi_l) \rangle$, as well as $\langle |S_{11}|^2 \rangle$, depend only on $|\rho_R|$ (and are independent of the phase of ρ_R). We have verified this by numerical simulation using the impedance matrix generated from (4.10) with up to seven channels.
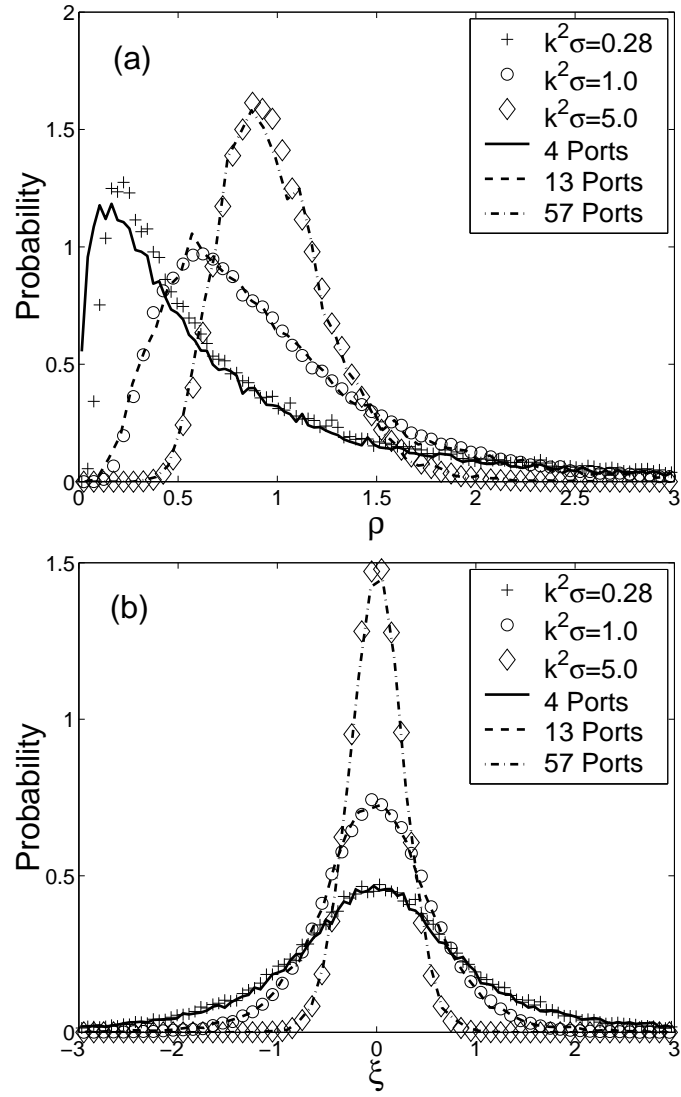
Figure 5.4: Comparison between the impedance obtained from the one-port lossy case and the multiple lossless case. (a) for the real part of the impedance; (b)for the imaginary part of the impedance.

Chapter 6

Variance Ratio of Impedance and Scattering Matrices

6.1 Introduction

Statistical variations of the elements of Z and S due to small random variations in the scattering are of great interest. These statistics have two fundamental influences, (i) universal aspects described by random matrix theory, and (ii) nonuniversal aspects dependent upon the details of the coupling of input channels (e.g., transmission lines) to the scatterer. Our main result concerns the quantity,

$$VR_z = \frac{Var[Z_{ij}]}{\sqrt{Var[Z_{ii}]Var[Z_{jj}]}}, \qquad i \neq j, \tag{6.1}$$

where $Var[A]$, the variance of the complex scalar A, is defined as the sum of $Var[ReA]$ and $Var[ImA]$. Our result is of the form

$$VR_z = \begin{cases} F_1(\lambda) & \text{for GOE,} \\ F_2(\lambda) & \text{for GUE,} \end{cases} \tag{6.2}$$

where λ is a parameter characterizing the losses within the scatterer. For example, in the case of an electromagnetic cavity, $\lambda = \omega/(2Q\Delta\omega)$, where ω is the
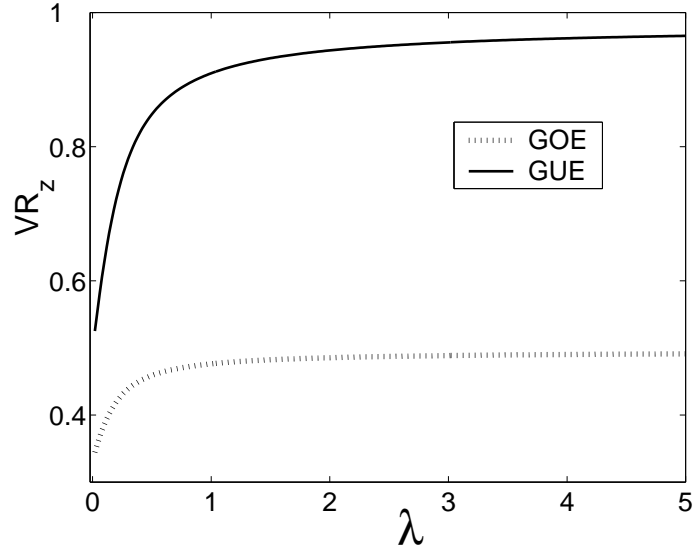
Figure 6.1: VR_z versus the loss parameter λ, as specified in Eq. (6.13) and Eq. (6.14).

frequency of the incoming signal, $\Delta\omega$ is the average spacing between cavity resonant frequencies near ω, and Q is the quality factor of the cavity ($Q = \infty$ if there are no internal losses).

The remarkable aspect of (6.2) is that $F_{1,2}(\lambda)$ depends only on the loss parameter and not on the nonuniversal properties of the coupling to the cavity. Thus VR_z is a universal function of the loss λ. The results for F_1 and F_2 (to be derived subsequently) are shown in Fig. 6.1. For $\lambda \gg 1$,

$$VR_z = \begin{cases} 1/2 & \text{for GOE,} \\ 1 & \text{for GUE.} \end{cases}, \tag{6.3}$$

and for $\lambda \ll 1$,

$$VR_z = \begin{cases} 1/3 & \text{for GOE,} \\ 1/2 & \text{for GUE.} \end{cases}. \tag{6.4}$$

78

A ratio similar to (6.1) can also be considered for the scattering matrix S,

$$VR_s \equiv \frac{Var[S_{ij}]}{\sqrt{Var[S_{ii}]Var[S_{jj}]}}, \qquad i \neq j. \qquad (6.5)$$

In contrast with (6.2), VR_s in general depends on *both* the coupling to the cavity and on the loss parameter λ. However, in the special case of high loss, VR_s becomes universal,

$$VR_s = \begin{cases} 1/2 & \text{for GOE,} \\ 1 & \text{for GUE.} \end{cases}, \qquad \lambda \gg 1 \qquad (6.6)$$

That is, $VR_s = VR_z$ for $\lambda \gg 1$. Based on their electromagnetics experiments, Fiachetti and Michelsen [72] have recently conjectured the universality of (6.6) in the GOE case. More generally, (6.6) follows from classic results of Hauser and Feshbach describing fluctuations in the cross section of inelastic neutron scattering [73], and this result has been obtained by Friedman and Mello [74] using the concept of maximization of information entropy, and by Agassi *et al.* [75] using a random-matrix model. The important point is that a universal result for VR_s [i.e., Eq. (6.6)] applies only for $\lambda \gg 1$, while the universal result for VR_z, Eq. (6.2) and Fig. 6.1, is for arbitrary λ.

In what follows we will derive these results. Section 6.2 derives the results for impedance variance ration, VR_z. Section 6.3 considers the scattering variance ratio.

6.2   Impedance Variance Ratio

We now obtain Eq. (6.2) for VR_z and discuss the result (6.6) for VR_s. We adopt the formulation we used in the previous chapters that incorporate the nonuniversal effects of the specific coupling geometry of input-output channels to the

scatterer, combined with the random matrix theory for the universal aspects of the chaotic wave behavior within the scatterer. (In what follows, we use terminology appropriate to microwave experiments.) In the GOE case, the impedance matrix Z is described by Eq. 4.8. The system dependent part of the coupling is characterized by the corresponding radiation impedance matrix $Z_r = R_r + jX_r$. In the case of ports that are far apart, e.g., of the order of the cavity size, the off-diagonal elements of Z_r are small and will be neglected. Thus we will take Z_r to be a diagonal matrix with elements $Z_{ri} = R_{ri} + jX_{ri}$.

We recall the construction of the Z matrix in the lossy case as follows,

$$
\begin{aligned}
Z_{ii} &= -\frac{j}{\pi} \sum_{n=1} \frac{R_{ri}\Delta_n w_{in}^2}{k^2(1 - jQ^{-1}) - k_n^2} \equiv R_{ii} + jX_{ii} \\
&= \frac{1}{\pi}\left[\sum_{n=1} \frac{R_{ri}\Delta_n w_{in}^2 k^2/Q}{(k^2 - k_n^2)^2 + (k^2/Q)^2} + j\sum_{n=1} \frac{R_{ri}\Delta_n w_{in}^2(k_n^2 - k^2)}{(k^2 - k_n^2)^2 + (k^2/Q)^2}\right].
\end{aligned}
\tag{6.7}
$$

Calculation of the moments of the impedance is facilitated by the fact that the eigenvalues and eigenfunctions in the chaotic cavities are statistically independent. For example, the expected value of X_{ii} is,

$$
\begin{aligned}
E[X_{ii}] &= \lim_{M\to\infty} \frac{1}{\pi} \sum_{n=1}^{M} \int dw_{in} f(w_{in}) w_{in}^2 \int dk_1^2 \cdots dk_M^2 \\
&\quad P_J(k_1^2, \cdots, k_M^2) \frac{R_{ri}\Delta_n(k_n^2 - k^2)}{(k^2 - k_n^2)^2 + (k^2/Q)^2},
\end{aligned}
\tag{6.8}
$$

where $f(w_{in})$ is the probability distribution function (pdf) of w_{in} and P_J is the joint pdf of the eigenvalues. Integrating over all k_j, $j \neq n$, we express $E[X_{ii}]$ as an integral over the pdf of k_n^2, $P_1(k_n^2) = 1/(\Delta_n M)$, we consider the $M \to \infty$ limit and use $\langle w_n^2 \rangle = 1$ for the Gaussian random variable w_n.

$$
E[X_{ii}] = \int dk_n^2 \frac{R_{ri}(k_n)(k_n^2 - k^2)/\pi}{(k^2 - k_n^2)^2 + (k^2/Q)^2} = X_{ri}(k).
\tag{6.9}
$$

The second equality in (6.9) relating $E[X_{ii}]$ to the radiation reactance requires $Q \gg 1$ and is analogous to the Kramers-Kronig relation.

The second moment of X_{ii} can be determined in a similar way by integrating over all j except $j = t, s$ and using the joint distribution function $P_2(k_t^2, k_s^2) = [1 - g(|k_t^2 - k_s^2|/\Delta)]/(M\Delta)^2$, where $g(|k_t^2 - k_s^2|/\Delta)$ is known from Random Matrix theory [22]. Assuming that the radiation resistance $R_{ri}(k_n)$ and the average spacing Δ_n vary slowly over the damping width k^2/Q, we obtain

$$Var[X_{ii}] = \frac{R_{ri}^2}{\lambda}[\frac{3}{2\pi} - \frac{1}{\pi}\int_0^\infty dx g(x)\frac{4}{4 + (x/\lambda)^2}], \tag{6.10}$$

where $\lambda = k^2/(Q\Delta)$. A similar moment evaluation can be carried out for R_{ii}, as specified in Eq. (6.7), which yields the same expression as Eq. (6.10) for $Var[R_{ii}]$. For GOE (the case we are now considering) we have that [22], $g(s) = f^2(s) - [\int_0^s d(s')f(s') - 1/2](df/ds)$, where $f(s) = [(sin\pi s)/(\pi s)]$.

In order to obtain the variance ratio, we also apply the previous process to the off diagonal term Z_{ij}, $i \neq j$, which, based on Eq. (4.8), is given by

$$\begin{aligned} Z_{ij} = \frac{1}{\pi}[&\sum_n \frac{\sqrt{R_{ri}R_{rj}}\Delta_n w_{in} w_{jn} k^2/Q}{(k^2/Q)^2 + (k^2 - k_n^2)^2} \\ &+ j\sum_n \frac{\sqrt{R_{ri}R_{rj}}\Delta w_{in} w_{jn} k^2/Q}{(k^2/Q)^2 + (k^2 - k_n^2)^2}]. \end{aligned} \tag{6.11}$$

Since w_{in} and w_{jn} are independent, the first moments of X_{ij} and R_{ij} are both zero, and the variance is equal to the second moment,

$$\begin{aligned} Var[X_{ij}] &= \lim_{M\to\infty} \frac{M}{\pi^2} \int dk_n^2 \frac{R_{ri}R_{rj}\Delta_n^2 \langle w_{in}^2 \rangle \langle w_{jn}^2 \rangle}{[(k_n^2 - k^2)^2 + (k^2/Q)]^2} P_1(k_n^2) \\ &= \frac{R_{ri}R_{rj}}{\lambda} \frac{1}{2\pi}, \end{aligned} \tag{6.12}$$

The same result is obtained for $Var[R_{ij}]$. Combining Eq. (6.12) with Eq. (6.10), we have Eq. (6.2) with

$$VR_z = F_1(\lambda) = [3 - 2\int_0^\infty dx g(x)\frac{4}{4 + (x/\lambda)^2}]^{-1}. \tag{6.13}$$

A similar calculation in the GUE case is facilitated by the simpler form of the function $g(x)$ which is now given by $g(x) = \sin^2(\pi x)/(\pi x)^2$. We obtain

$$VR_z = F_2(\lambda) = [2 - 2\int_0^\infty dx(\frac{\sin \pi x}{\pi x})^2 \frac{4}{4 + (x/\lambda)^2}]^{-1}$$
$$= [1 + \frac{1 - e^{-4\pi\lambda}}{4\pi\lambda}]^{-1}. \tag{6.14}$$

We note that the two-frequency correlation functions for the elements of the impedance and the scattering matrix have recently been calculated by Savin, Fyodorov and Sommers [76], and are consistent with the preceding in the limit of zero frequency separation.

6.3   Scattering Variance Ratio

We now consider the scattering matrix in the high loss limit, $\lambda \gg 1$. For simplicity, we consider the case of two channels connecting to the scatterer, $N = 2$, and Z and S are 2×2 matrices. We note that a chaotic scattering process can be divided into a direct process and a delayed process, which leads to a separation of the mean part (equal to Z_r) and the fluctuating part δZ of the cavity impedance, $Z = Z_r + \delta Z$. The fluctuating part δZ decreases as loss increases. Thus in the high loss limit, $\delta Z \ll Z_r$, which implies $Z_{12}, Z_{21} \ll Z_{11}, Z_{22}$. (Recall, the mean parts of the off diagonal components are zero.) We may now form S using $S = Z_0^{-1/2}(Z - Z_0)(Z + Z_0)^{-1}Z_0^{1/2}$. Since the off diagonal terms of Z are small, the diagonal components of S are dominated by the diagonal components of Z. We then find for S_{11},

$$S_{11} \cong \frac{Z_{11} - Z_{01}}{Z_{11} + Z_{01}} = \frac{(Z_{r1} - Z_{01}) + \delta Z_{11}}{(Z_{r1} + Z_{01}) + \delta Z_{11}}$$
$$\cong S_{r1} + [\frac{2Z_{01}}{(Z_{r1} + Z_{01})^2}]\delta Z_{11}, \tag{6.15}$$

where $S_{r1} = (Z_{r1} - Z_{01})/(Z_{r1} + Z_{01})$, and Z_{01} is the characteristics impedance of channel 1. Thus, we obtain

$$Var[S_{11}] = |\frac{2Z_{01}}{(Z_{r1} + Z_{01})^2}|^2 Var[Z_{11}]. \tag{6.16}$$

In addition, we can express S_{12} in the high damping limit as

$$S_{12} = \frac{2Z_{12}\sqrt{Z_{01}Z_{02}}}{(Z_{11} + Z_{01})(Z_{22} + Z_{02})} \simeq \frac{2Z_{12}\sqrt{Z_{01}Z_{02}}}{(Z_{r1} + Z_{01})(Z_{r2} + Z_{02})}, \tag{6.17}$$

which leads to

$$Var[S_{12}] = |\frac{2\sqrt{Z_{01}Z_{02}}}{(Z_{r1} + Z_{01})(Z_{r2} + Z_{02})}|^2 Var[Z_{12}], \tag{6.18}$$

and similarly for $Var[S_{21}]$. Combining Eq. (6.16) and Eq. (6.18), we recover Eq. (6.6) and we note that this result is independent of the coupling (i.e., independent of Z_r).

To illustrate the influence of coupling on VR_s at finite loss parameter λ, we consider the impedance matrix in the GOE case using the model normalized impedance ζ used in chapter 4, $Z = R_r^{1/2}\zeta R_r^{1/2} + jX_r$, where ζ is given by $\zeta_{ij} = -(j/\pi)\sum_{n=1}^{M}(w_{in}w_{jn})/(\tilde{k}^2 - \tilde{k}_n^2 - j\lambda)$, $\tilde{k}_n^2 = k^2/\Delta$, and $\tilde{k}^2$ is set to be $M/2$, such that mean of ζ is zero. We express a model scattering matrix S as

$$S = (\gamma_r^{1/2}\zeta\gamma_r^{1/2} + j\gamma_x + 1)^{-1}(\gamma_r^{1/2}\zeta\gamma_r^{1/2} + j\gamma_x - 1), \tag{6.19}$$

where $\gamma_r = Z_0^{-1}R_r$ and $\gamma_x = Z_0^{-1}X_r$, When γ_r is the identity matrix and γ_x is zero, we reach the so-called perfect coupling condition, which means that the scattering is determined by the delayed process and the direct process is absent. We now consider an example in which the two port couplings are the same so that $\gamma_{r,x} = diag(\bar{\gamma}_{r,x}, \bar{\gamma}_{r,x})$, where $\bar{\gamma}_{r,x}$ is a scalar. Figures 6.2(a) and (b) show results for the variation of VR_s with the coupling parameters $\bar{\gamma}_r$ and $\bar{\gamma}_x$, for a high loss

case ($\lambda = 5$) and for the lossless case ($\lambda = 0$). In Fig. 6.2(a), we fix $\bar{\gamma}_x$ to be zero, and vary $\bar{\gamma}_r$, while in Fig. 6.2(b), $\bar{\gamma}_r$ is fixed to be 1 and $\bar{\gamma}_x$ is varied. Compared to the high damping case, VR_s in the lossless case has a much larger deviation from the constant 1/2. Note that VR_s is 1/2 in the perfect-coupling case (i.e., $\bar{\gamma}_r = 1$, $\bar{\gamma}_x = 0$), no matter whether the cavity is highly lossy or lossless. This is again related to the concept of "weak localization" mentioned in Chapter 5. In the perfect coupling case, the S matrices can be described by Dyson's ensemble and the ensemble of S matrices is invariant to unitary transformations. This implies to a zero mean value of the S matrix, therefore, the variance of S elements is also its second moment. In other words, $VR_s = 1/2$ is equivalent to $\langle |S_{ii}|^2 \rangle = 2 \langle |S_{ij}|^2 \rangle$.

In the case of an N-port we can think of the above two port consideration of VR_s as applying to the N-port converted to a two port by opening channels $3, 4, \cdots, N$; i.e., the incoming waves $a_3, a_4, \cdots a_N$ are identically zero (for a microwave cavity with transmission line inputs, this corresponds to terminating transmission lines $3, 4, \cdots, N$ with their characteristic impedances, $Z_{03}, Z_{04}, \cdots, Z_{0N}$). Thus ports $3, 4, \cdots, N$ effectively add to the loss due to the energy flux leaving through them. If the ports $3, 4, \cdots, N$ are assumed to act like distributed loss, they can be taken into account by increasing the loss parameter λ. [This increased loss enhances the validity of Eq. (6.6).]

Experimental results testing the theoretical predictions for the statistical fluctuations in the variance of the S and Z elements have been reported, in the limit of large damping [77]. These experiments are done in an air-filled, quarter bow-tie shaped cavity which acts as a two-dimensional resonator below 19 GHz [78]. This cavity has previously been used for the successful study of the eigenvalue spacing statistics [79], eigenfunction statistics [36], and for studying the universal
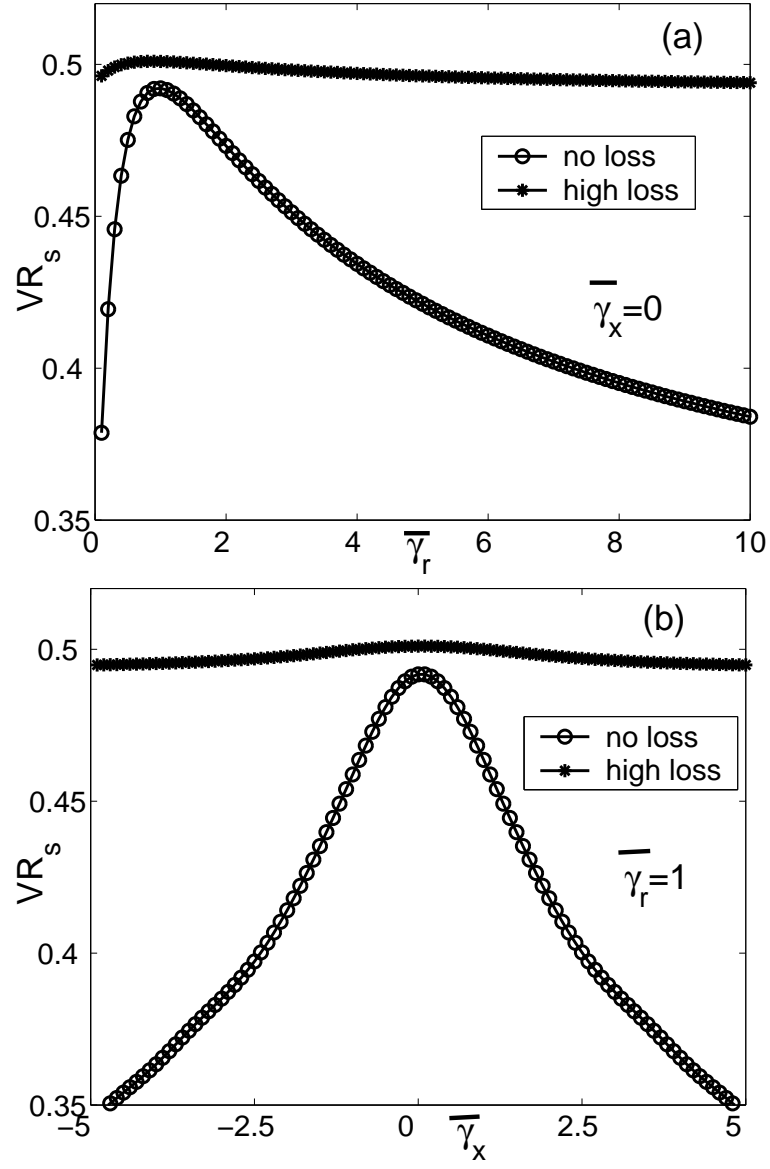
Figure 6.2: (a) VR_s versus $\bar{\gamma}_r$ for $\bar{\gamma}_x = 0$ in the lossless case $\lambda = 0$ and in a high loss case $\lambda = 5$. (b)VR_s versus $\bar{\gamma}_x$ for $\bar{\gamma}_r = 1$.

fluctuations in the impedance [16] and scattering matrix [64] for a wave chaotic system. The cavity is driven by two ports; and has a typical loaded Q of about 200 in the frequency range 7.2 GHz to 8.4 GHz from a direct S_{21} measurement. This translates to a damping parameter of $\lambda >\sim 1$ for the frequency range of this experiment. Experimentally averaged values of VR_z and VR_s agree well with our prediction to be 0.5 over the frequency range 4GHz to 12GHz.

Chapter 7

Summary and Future Work

7.1 Summary

We have applied the concepts of wave chaos to the problem of characterizing the statistics of the impedance and scattering matrices for irregular electromagnetic cavities in the small wavelength regime. The coupling of energy in and out of the port in such cavities depends on both the geometry of the port and the geometry of the cavity. We found that these effects can approximately be separated. The geometry of the port is characterized by its radiation impedance which describes the port in the case in which the distant walls of the cavity are treated as perfect absorbers (or else are removed to infinity) and can be determined by non-statistical measurements [16]. Assuming chaotic ray trajectories, the effects of the geometry of the cavity can be treated in a statistical way using Random Matrix Theory. A linear relation between cavity impedance and the corresponding radiation impedance is given in Eq. (3.4), and in Eq. (4.22) for the general lossy case. Thus we are able to extract a universal normalized impedance ζ, hence a normalized scattering matrix.

Our model predicts that, in the lossless case, the impedance is Lorentzian

distributed with a mean equal to the radiation reactance and a width equal to the radiation resistance. The negative correlation between impedances in different channels, as shown in Fig. 4.1, agrees well with Dyson's circular ensemble (4.12). There is an obvious difference between the cases in which time reversal symmetry is preserved(TRS) or broken(TRSB). One of the major consequences is the difference in the averaged reflection/transmission coefficients for the TRS and TRSB cases. The coherence of ray trajectories enhances the strength of reflection coefficients and gives rise to what is known as "weak localization". We further incorporate two coupling parameters γ_R and γ_X into the formulation of multiport scattering matrices and find that $|\rho_R|$, which is a function of the two parameters above, characterizes the transport process. This finding makes it possible to engineer the wave transport and field distribution in a predefined way.

Effects of distributed loss are also investigated, and we have generated pdf's for the real and imaginary parts of the universal normalized impedance ζ. In addition, explicit calculations are given for their variances and covariance, depending on the loss parameter and general class of symmetry of the system. The distribution of ζ is the same under variation of the coupling (e.g., interposing a lossless two-port extension at the input), and could serve as a reliable characterization of the loss parameter and and of the crossover from TRS to TRSB. Another possible characterization is the variance ratio between diagonal elements and off-diagonal elements of Z and S matrix. In particular, the impedance variance ratio is a universal function of the loss in the scatterer, as shown in Eqs. (6.13), (6.14).

Using HFSS, we test the conclusions above on impedance and scattering data calculated from direct numerical solution of Maxwell Equations. The agreement between the numerical results and the theoretical predictions convinces us that

our theory successfully recovers the statistical ensemble for chaotic scattering.

7.2 Future Work

7.2.1 Closely Spaced Ports

Most of our numerical simulations and microwave experiments are done in the cases that ports are sufficiently far apart and only one mode is allowed in each input channel. Thus the "direct talk" between different channels could be neglected. In other words, the radiation impedance characterizing the coupling is assumed to be diagonal. Though, with the argument given in section 4.1, we believe our model is still valid even when the two ports are spaced within a distance of the order of the wavelength, a direct numerical and experimental proof would be highly desired .

7.2.2 Effects of Scars

Computations of wave solutions for eigenmmodes of chaotic cavities show finite wavelength induced deviations from the random plane wave hypothesis. These deviations manifest themselves as regions of enhanced wavefunction magnitude in the vicinity of unstable periodic ray orbits embedded in the chaotic phase space. These enhancements are called 'scars', and have been discussed in Sec. 1.2.4. While it is likely that, in some appropriate sense, the effect of scaring goes away in the asymptotic limit of vanishing wavelength, scars may lead to noticeable effects in small wavelength situations. Thus we wonder whether the discrepancies between the numerical results and theoretical prediction shown in Fig. 3.3 and Fig. 5.1 are due to scars. Scaring is difficult to include in our approach, since it is

89

highly system dependent, and cannot be addressed in the frame of random matrix theory. On the other hand, scaring is of great interest to practical applications, for instance, to protect electronics circuits from unusually high intensity fields.

7.3 Conclusion

Much progress has been made to enhance our understanding of statistical properties of impedance and scattering matrices. In particular, we have had success in modelling the system-dependent coupling and the universal aspects of wave behaviors, characterized by an appropriate loss parameter, and in predicting the wave transport efficiency. We have high hopes that this model will be further developed and contribute much of value to the realms of both basic understanding and practical application.

Appendix A

Evaluation of the Radiation Impedance in

Annular Current Profile

In this appendix we derive the radiation impedance corresponding to the current distribution profile $u(x, y) = \pi^{-1}\delta(x^2 + y^2 - a^2)$. Inserting this function into Eq. (2.13) and Fourier transforming in x and y with transform variable $\vec{k}_n$ we have

$$(k^2 - k_n^2)\bar{V}_T(\vec{k}_n) = -jkh\eta_0 \hat{I} \int d^2\vec{r}\, \frac{\delta(r - a)}{2\pi a} e^{-j\vec{k}_n \cdot \mathbf{r}}, \tag{A.1}$$

where $\bar{V}_T(\vec{k}_n)$ is the Fourier transform of $\hat{V}_T$. The right hand side of (A.1) can be evaluated making use of the identity,

$$\int_0^{2\pi} \frac{d\phi}{2\pi} e^{-jk_n a \cos\phi} = J_0(k_n a). \tag{A.2}$$

The result is,

$$\bar{V}_T(\vec{k}_n) = -\frac{jkh\eta_0 J_0(k_n a)}{k^2 - k_n^2}\hat{I}. \tag{A.3}$$

The port voltage is given by Eq. (2.14) and may be evaluated using Parseval's theorem,

$$\hat{V} = \int d^2\vec{r}\, u(\vec{r})\hat{V}_T(\vec{r}) = \int \frac{d^2\vec{k}_n}{(2\pi)^2}\hat{V}_T(\vec{k}_n) J_0(k_n a), \tag{A.4}$$

where $d^2\vec{k}_n = d\phi k_n dk_n$ and ϕ is the angle of $\vec{k}_n$. This gives $\hat{V} = Z_R \hat{I}$ where

$$Z_R = -jkh\eta_0 \int \frac{d^2\vec{k}_n}{(2\pi)^2} \frac{J_0^2(k_n a)}{k^2 - k_n^2}.$$ (A.5)

This has the form of Eq. (2.24) if we identify

$$R_R(k_n) = \frac{kh\eta_0}{4} J_0^2(k_n a)$$ (A.6)

as the radiation resistance.

Appendix B

Lorentzian distribution for ξ

In this appendix we discuss the probability density distribution for ξ in Eq. (3.5)

$$\xi = \sum_{n=1}^{N} \eta_n, \tag{B.1}$$

where $\eta_n = -w_n^2/[\pi(k^2 - k_n^2)]$ and we have dropped the superscribed tilde on the notation for the normalized wavenumber. In Eq. (B1) the w_n are Gaussian random variables with zero mean and unit variance, and, for a Poisson level distribution, each of the values k_n^2 are independently uniformly distributed in the interval $[0, N]$. This prescription maintains the mean spacing between k_n^2 values at unity. With this assumption on the statistics of k_n^2 and w_n the variables η_n are independent and identically distributed. Therefore, $P_\xi(\xi)$, the probability density function of ξ, is

$$P_\xi(\xi) = \int d\eta_1 .. d\eta_N \delta(\xi - \sum_n \eta_n) \prod_{i=1}^{N} P_\eta(\eta_i). \tag{B.2}$$

We will investigate the characteristic function of the random variable ξ, i.e. the Fourier transformation of $P_\xi(\xi)$,

$$\bar{P}_\xi(t) = \int d\eta_1 .. d\eta_N e^{-jt \sum_n \eta_n} \prod_{i=1}^{N} P_\eta(\eta_i) = [\bar{P}_\eta(t)]^N, \tag{B.3}$$

where

$$\bar{P}_\eta(t) = \int d\eta e^{-jt\eta} P_\eta(\eta)$$

$$= \int_{-\infty}^{\infty} dw \frac{1}{\sqrt{2\pi}} exp(-\frac{w^2}{2}) \int_0^N \frac{dk_n^2}{N} \int d\eta e^{-jt\eta} \delta[t - \frac{w^2/\pi}{k^2 - k_n^2}] \qquad \text{(B.4)}$$

$$= \int_0^N \frac{dk_n^2}{N} \frac{1}{[1 + 2j\frac{t}{\pi}\frac{1}{k^2-k_n^2}]^{-\frac{1}{2}}}.$$

Note that $\bar{P}_\eta(-t) = \bar{P}_\eta^*(t)$ from the reality condition, so it is sufficient to evaluate the integral above for the case of positive t.

The integrand in (B4) has singularities of $k_n^2 = k^2$ and $k_n^2 = k^2 + 2jt/\pi$. The integration contour (defined to be along the real k_n^2 axis) passes through the singularity at $k_n^2 = k^2$. However, this singularity is weak, $(k^2 - k_n^2)^{1/2}$, and we can regard the contour as passing below the singularity. Thus, for $t > 0$ we may deform the integration contour into a large semicircle in the lower half k^2 plane starting at $k_n^2 = 0$ and ending at $k_n^2 = N$. For each point on this contour $2t/[\pi(k_n^2 - k^2)]$ is small and we can Taylor expand the integrand for $|k_n^2 - k^2| \sim N$

$$\bar{P}_\eta(t) = \frac{1}{N} \int_0^N dk_n^2 [1 - \frac{j}{2}\frac{2t}{\pi(k_n^2 - k^2)}] + O(\frac{t^2}{N^2})$$

$$= 1 - \frac{t}{N} - j\frac{t}{\pi N} \log|\frac{N - k^2}{k^2}| + O(t^2/N^2). \qquad \text{(B.5)}$$

The sign of the term $-t/N$ is determined by deforming the contour into the lower half plane below the pole $k_n^2 = k^2$. In the limit of $N \to \infty$ we may drop the term $O(t^2/N^2)$. Also, recalling the reality condition $\bar{P}_\eta(-t) = \bar{P}_\eta^*(t)$, (B5) yields

$$\bar{P}_\eta(t) \cong 1 - \frac{|t|}{N} - j\frac{t}{\pi N} \log|\frac{N - k^2}{k^2}|, \qquad \text{(B.6)}$$

Therefore, $\bar{P}_\xi(t)$ is:

$$\bar{P}_\xi(t) = [1 - \frac{|t|}{N} - j\frac{t}{\pi N} \log|\frac{N - k^2}{k^2}|]^N$$

$$= \exp[-|t| - j\frac{t}{\pi} \log|\frac{N - k^2}{k^2}|]. \qquad \text{(B.7)}$$

Taking the inverse Fourier transform in t we find that ξ is a Lorentzian distributed random variable with unit characteristic width and a mean value $\log |(N - k^2)/k^2|/\pi$.

Appendix C

Variance of Cavity Reactance and Resistance in the Lossy Case.

From Eq. (4.17), we obtain the expression for the complex impedance in the single port case,

$$Z(\sigma) = \frac{1}{\pi} \sum_{1}^{N} [\frac{\Delta(k_n^2)R_R(k_n^2)w_n^2[k_d^2 + j(k_n^2 - k^2)]}{(k^2 - k_n^2)^2 + (k_d^2)^2}]$$
$$= R(\sigma) + jX(\sigma),$$
(C.1)

where Δ is the mean spacing $\langle k_n^2 - k_{n-1}^2 \rangle$, $X(\sigma)$ and $R(\sigma)$ are cavity reactance and resistance in the lossy case and $k_d^2 = k^2\sigma$. In this appendix, we are going to evaluate the mean and variance of $X(\sigma)$ and $R(\sigma)$ as well as their covariance.

We first investigate the mean of $R(\sigma)$. We express the mean in terms of probability distribution function for the eigenvalues k_n^2.

$$E[R(\sigma)] = \frac{1}{\pi} \int \ldots \int dk_1^2 \ldots dk_N^2 P_J(k_1^2, \ldots, k_N^2)$$
$$\sum_{n'=1}^{N} \frac{R_R \Delta \langle w_{n'}^2 \rangle k_d^2}{(k^2 - k_{n'}^2)^2 + k_d^4},$$
(C.2)

where P_J is the joint distribution of eigenlevels $(k_1^2, \ldots, k_N^2)$ assuming they are unordered. Since the levels are not ordered, in each term of the sum, we can

integrate over all $k_n^2 \neq k_{n'}^2$, and obtain N identical terms. Thus,

$$E[R(\sigma)] = \frac{N}{\pi} \int dk_{n'}^2 P_1(k_{n'}^2) R_R \Delta \langle w^2 \rangle \frac{k_d^2}{(k^2 - k_{n'}^2)^2 + k_d^4} \quad \text{(C.3)}$$

where $P_1(k_{n'}^2)$ is distribution for a single level. Here we have introduced an integer N representing the total number of levels. We will take the limit of $N \to \infty$. The single level probability distribution then satisfies by definition,

$$P_1(k_{n'}^2) = \frac{1}{N \Delta(k_{n'}^2)}. \quad \text{(C.4)}$$

We next assume that the radiation resistance $R_R(k_{n'}^2)$ is relatively constant over the interval of $k_{n'}^2$ values satisfying $|k^2 - k_{n'}^2| < k_d^2$ and we will move it outside the integral replacing it by $R_R(k^2)$. Assuming that k_d^2 is not too large ($k_d^2 \ll k^2$) we can take the end points at the integral to plus and minus infinity and evaluate Eq. (C.3) as

$$E[R] = \frac{R_R}{\pi} \int_{-\infty}^{\infty} dx \frac{1}{x^2 + 1} = R_R(k^2), \quad \text{(C.5)}$$

where $x = (k_{n'}^2 - k^2)/k_d^2$. Thus the expected value of the real part of cavity impedance is the radiation resistance independent of the amount of damping. This is somewhat surprising since we have previously asserted that in the lossless case, the cavity resistance is zero. The constancy of the expected resistance results from the resonant nature of the cavity impedance. When losses are small, $k^2 \sigma = k_d^2 \ll 1$, for almost all frequencies the resistance is small. However, for the small set of the frequencies near a resonance the resistance is large. This is evident in the histograms of Fig. (4.3b). The result is that small chance of a large resistance and large chance of small resistance combine to give an expected value resistance which is constant.

In order to obtain the variance of $R(\sigma)$, we calculate the second moment of

97

$R(\sigma)$,

$$E[R(\sigma)^2] = (\frac{1}{\pi})^2 \int \ldots \int dk_1^2 \ldots dk_N^2 P_J(k_1^2, \ldots, k_N^2)$$

$$\sum_{n',m'=1}^{N} \frac{\Delta^2 R_R(k_{n'}^2) R_R(k_{m'}^2) \langle w_{m'}^2 w_{n'}^2 \rangle k_d^4}{((k^2 - k_{m'}^2)^2 + k_d^4)((k^2 - k_{n'}^2)^2 + k_d^4)} \tag{C.6}$$

$$\equiv I_1 + I_2.$$

Following the arguments advanced to calculate $E[R(\sigma)]$, we note that there will be N terms in the double sum for which $k_{n'}^2 = k_{m'}^2$ giving

$$I_1 = \frac{N}{\pi^2} \int dk_{n'}^2 P_1(k_{n'}^2) \frac{\Delta^2 R^2(k_{n'}^2) \langle w_{n'}^4 \rangle k_d^4}{[(k^2 - k_{n'}^2)^2 + k_d^4]^2} \tag{C.7}$$

and $N(N-1)$ terms for which $k_{m'}^2 \neq k_{n'}^2$ giving

$$I_2 = N(N-1) \iint dk_{n'}^2 dk_{m'}^2$$

$$\frac{P_2(k_{n'}^2, k_{m'}^2) \Delta(k_{n'}^2) \Delta(k_{m'}^2 R_R(k_{n'}^2) R_R(k_{m'}^2) \langle w_{n'}^2 \rangle \langle w_{m'}^2 \rangle k_d^4}{[(k^2 - k_{n'}^2)^2 + k_d^4][(k^2 - k_{m'}^2)^2 + k_d^4]}. \tag{C.8}$$

For the first integral we use (C.4) for the single level distribution function, and making the same approximation as before, we obtain

$$I_1 = R_R^2(k^2) \frac{\langle w^4 \rangle \Delta(k^2)}{2\pi k_d^2}. \tag{C.9}$$

For the second integral we need to introduce the two level distribution function. For the spectra that we consider, the two level distribution has the form

$$P_2(k_{n'}^2, k_{m'}^2) = (\frac{1}{N\Delta})^2 [1 - g(|k_{n'}^2 - k_{m'}^2|)]. \tag{C.10}$$

Here the function g describes the correlations between two energy levels. For uncorrelated levels giving a Poisson distribution of spacings we have $g = 0$. In the presence of level repulsion we expect $g(0) = 1$ with $(1-g) \propto |k_{n'}^2 - k_{m'}^2|^\beta$ for small spacing, and $\beta = 1$ for TRS and $\beta = 2$ for TRSB systems. As $|k_{n'}^2 - k_{m'}^2| \to \infty$, $g \to 0$ indicating loss of correlation for two widely separated levels. The function g

will be different for spectra produced by random matrices and spectra generated from sequences of independent spacings. Expressions of g for the spectra of random matrices can be found in the book by Mehta ([22], Ch. 5 & 6). We will derive the expression for g for spectra generated by sequences of independent spacings later in this appendix.

Based on expression (C.10) and the usual assumptions on the slow variations of R_R and Δ with eigenvalue $k_{n'}^2$, we obtain

$$I_2 = (E[R])^2 - I_g, \tag{C.11}$$

where the first term comes from the 1 in C.10 and the second term comes from the correlation function g

$$I_g = \frac{R_R(k^2)\langle w^2 \rangle^2}{\pi} \int_{-\infty}^{\infty} \frac{d\tilde{k}^2}{k_d^2} \frac{2}{4 + (\tilde{k}^2/k_d^2)^2} g(|\tilde{k}^2|). \tag{C.12}$$

The variance of R is thus given by

$$\begin{aligned} Var[R] &= E[R]^2 - E[R^2] \\ &= \frac{R_R^2}{\pi} \frac{\Delta}{k_d^2} [\frac{\langle w^4 \rangle}{2} - \langle w^2 \rangle^2 \int_{-\infty}^{\infty} \frac{d\tilde{k}^2}{\Delta} \frac{2g(|\tilde{k}^2|)}{4 + (\tilde{k}^2/k_d^2)^2}]. \end{aligned} \tag{C.13}$$

Note, since w is a Gaussian random variable with zero mean and unit variance, $\langle w^2 \rangle = 1$ and $\langle w^4 \rangle = 3$.

Equation (C.13) shows that the variances of R depends on k_d^2/Δ, the ratio of the damping width to the mean spacing of eigenvalues. In the low damping case, $k_d^2/\Delta \ll 1$, the integrand in (C.13) is dominated by the values of $|\tilde{k}^2| < \Delta$ and we replace g by its value $g(0)$. Doing the integral we find

$$Var[R] = R_R^2 [\frac{\Delta}{k_d^2} \frac{\langle w^4 \rangle}{2\pi} - g(0)\langle w^2 \rangle^2]. \tag{C.14}$$

Since the damping is small, the first term dominates and the variance is independent of the eigenvalue correlation function. This is consistent with our previous

findings that the eigenvalue statistics did not affect the distribution of reactance values.

In the high damping limit, $k_d^2 > \Delta$, the integral in (C.13) is dominated by $\tilde{k}^2$ values of order Δ and we have,

$$Var[R] = \frac{R_R^2}{\pi} \frac{\Delta}{k_d^2} [\frac{3}{2} - \int_0^\infty \frac{d\tilde{k}^2}{\Delta} g(|\tilde{k}^2|)].$$ (C.15)

The variance decreases as damping increases with a coefficient that depends on the correlation function. Physically the correlations are important because in the high damping case a relatively large number of terms in the sum (C.1) contribute to the impedance and the sum is sensitive to correlations in these terms.

The integral of the correlation function can be evaluated for different spectra. For spectra generated from random matrices, we have ([22], Ch.6)

$$g(s) = f(s)^2 - \frac{\partial f}{\partial s} [(\int_0^s ds' f(s')) - \frac{1}{2} sgn(s)]$$ (C.16)

for TRS matrices and

$$g(s) = f(s)^2$$ (C.17)

for TRSB matrices, where $f(s) = \sin(\pi s)/(\pi s)$. In both cases, we find

$$\int_0^\infty ds g(s) = \frac{1}{2}.$$ (C.18)

However, to consider the TRSB case we need to repeat the calculation including complex values of the Gaussian variable w. The result is

$$Var[R(\sigma)] = \frac{R_R^2}{\pi} \frac{\Delta}{k_d^2} [1 - \int_0^\infty \frac{d\tilde{k}^2}{\Delta} g(|\tilde{k}^2|)].$$ (C.19)

For spectra generated by sequences of independent spacing distributions we will show

$$\int_0^\infty \frac{d\tilde{k}^2}{\Delta} g(|\tilde{k}^2|) = 1 - \frac{1}{2} \langle s^2 \rangle,$$ (C.20)

where $\langle s^2 \rangle$ is the expected value for the normalized nearest neighbor spacing squared. Using (1.3) and (1.4), this gives

$$\int_0^\infty \frac{d\tilde{k}^2}{\Delta} g(|\tilde{k}^2|) = \begin{cases} 1 - \frac{2}{\pi} & \text{for TRS,} \\ 1 - \frac{3\pi}{16} & \text{for TRSB.} \end{cases} \tag{C.21}$$

Note also that (C.20) gives the required value of zero for Poisson spacing distributions, where $\langle s^2 \rangle = 2$.

We can evaluate the expected value of the reactance and its variance, as well as the covariance of reactance and resistance, using the same approach. We find the expected value of reactance is given by the radiation reactance,

$$E[X] = X_R(k^2). \tag{C.22}$$

The variance of the reactance is equal to that of the resistance (C.13) the covariance between them is zero.

We now derive the g-integral (C.20) for spectra generated from independent spacings. We introduce a conditional distribution $P_m(s)$ that is the probability density that the mth eigenvalue is in the range $[s, s+ds]$ given that eigenvalue $m = 0$, is at zero. For convenience, here s is the normalized spacing with unit mean. When $m = 1$, $P_1(s)$ is the spacing distribution $p(s)$. Thus, $1 - g(s)$ stands for the probability that there exists an eigenlevel at [s, s+ds] given one level located at 0. This equality can be expressed as the summation of $P_m(s)$,

$$1 - g(s) = \sum_{m=1}^\infty P_m(s). \tag{C.23}$$

$P_m(s)$ can be evaluated assuming the spacings are independent,

$$1 - g(s) = \sum_{m=1}^\infty [\int \prod_{i=1}^m ds_i P_1(s_i)\delta(s - \sum_{i=1}^m s_i)]. \tag{C.24}$$

101

We Laplace transform both sides of Eq. (C.24), and obtain

$$\frac{1}{\tau} - \int_0^\infty dse^{-\tau s}g(s) = \sum_{m=1}^\infty [\bar{P}_1(\tau)]^m = \frac{\bar{P}_1(\tau)}{1 - \bar{P}_1(\tau)}. \qquad (C.25)$$

To evaluate $\int_0^\infty dsg(s)$, we take the limit of $\tau \to 0$. The transform $\bar{P}_1(\tau)$ can be expressed in terms of the moments of $P_1(s)$,

$$\begin{aligned}
\bar{P}_1(\tau) &= \int_0^\infty e^{-s\tau} P_1(s)ds, \\
&\sim \int_0^\infty (1 - s\tau + \frac{s^2\tau^2}{2})P_1(s)ds, \qquad (C.26) \\
&= 1 - \tau\langle s \rangle + \frac{\tau^2}{2}\langle s^2 \rangle.
\end{aligned}$$

Thus, we can evaluate the integration of $g(s)$ to be

$$\begin{aligned}
\int_0^\infty dsg(s) &= \lim_{\tau \to 0} \int_0^\infty dse^{-\tau s}g(s) \\
&= \lim_{\tau \to 0}[\frac{1}{\tau} - \frac{\bar{P}_1(\tau)}{1 - \bar{P}_1(\tau)}] \qquad (C.27) \\
&= 1 - \frac{1}{2}\langle s^2 \rangle,
\end{aligned}$$

which is Eq. (C.20).

Appendix D

Evaluation of $\langle |S_{11}|^2 \rangle$ for a Two-port Cavity

In this appendix, we will start from the one-port case, and obtain an expression for the phase of S in term of the reflection coefficient ρ_R defined in Eq. (5.4). Then, using Eq. (4.12), we can evaluate $\langle \cos(\phi_1 - \phi_2) \rangle$ for the two-port in the TRS and TRSB cases.

In the one-port case, S can be expressed as

$$
\begin{aligned}
S = e^{j\phi} &= \frac{Z - Z_0}{Z + Z_0} \\
&= \frac{j(\gamma_X + \tilde{\xi}\gamma_R) - 1}{j(\gamma_X + \tilde{\xi}\gamma_R) + 1},
\end{aligned}
\tag{D.1}
$$

where $\tilde{\xi}$ is a zero mean, unit width, Lorentzian random variable, which can be written as,

$$
\tilde{\xi} = \tan\theta
\tag{D.2}
$$

with θ uniformly distributed in $[-\pi/2,\ \pi/2]$. Putting Eq. (D.2) into Eq. (D.1), we get

$$
e^{j\phi} = \frac{(\gamma_R + j\gamma_X - 1)e^{j\theta} - (\gamma_R - j\gamma_X + 1)e^{-j\theta}}{(\gamma_R + j\gamma_X + 1)e^{j\theta} - (\gamma_R - j\gamma_X - 1)e^{-j\theta}}.
\tag{D.3}
$$

Introducing ρ_R such that

$$
\gamma_R + j\gamma_X - 1 = \rho_R(\gamma_R + j\gamma_X + 1),
\tag{D.4}
$$

and defining

$$e^{-j\alpha} = \frac{\gamma_R - j\gamma_X + 1}{\gamma_R + j\gamma_X + 1}, \tag{D.5}$$

we obtain a compact expression for ϕ in term of θ and ρ_R,

$$e^{j\phi} = \frac{\rho_R - e^{-j(2\theta+\alpha)}}{1 - \rho_R^* e^{-j(2\theta+\alpha)}}$$
$$= e^{j\phi_R} e^{-j2\theta'} \frac{1 + |\rho_R| e^{j2\theta'}}{1 + |\rho_R| e^{-j2\theta'}}, \tag{D.6}$$

where $2\theta' = (2\theta + \alpha + \pi + \phi_R)$. Since α and ϕ_R depend only on the coupling coefficient γ_R and γ_X, and 2θ is uniformly distributed in $[0, \ 2\pi]$, the angle $2\theta'$ is also uniform in $[0, 2\pi]$. Thus,

$$P_\phi(\phi) = P_{2\theta'}(2\theta') \left| \frac{d(2\theta')}{d\phi} \right|$$
$$= \frac{1}{2\pi} \frac{1}{1 + |\rho_R|^2 - 2|\rho_R| \cos(\phi - \phi_R)}. \tag{D.7}$$

The relation between ϕ and $2\theta'$ also holds true for multi-port cases. Furthermore, from the joint probability density function of $2\theta_1$ and $2\theta_2$ in Eq. (4.12), which is only a function of the difference of two angles, we find that $2\theta_1'$ and $2\theta_2'$ have the same joint distribution specified in Eq. (4.12). Thus we can evaluate

$$\langle \cos(\phi_1 - \phi_2) \rangle = Re[e^{j\phi_1 - j\phi_2}]$$
$$= Re[\frac{e^{-j2\theta_1'} + |\rho_R|}{1 + |\rho_R| e^{-j2\theta_1'}} \frac{e^{j2\theta_2'} + |\rho_R|}{1 + |\rho_R| e^{j2\theta_2'}}], \tag{D.8}$$

by using the joint distribution of $2\theta_1'$ and $2\theta_2'$, $P_\beta(2\theta_1, 2\theta_2) \propto |e^{j2\theta_1'} - e^{j2\theta_2'}|^\beta$, where $\beta = 1$ corresponds to the TRS case, and $\beta = 2$ for TRSB case.

Introducing $\psi_1 = 2\theta_1'$, $\psi_2 = 2\theta_2'$, and their difference $\psi_- = \psi_1 - \psi_2$, we obtain

for the average of $\cos(\phi_1 - \phi_2)$,

$$
\langle\cos(\phi_1 - \phi_2)\rangle = \iint \frac{d\psi_1 d\psi_2}{(2\pi)^2} P(\psi_1, \psi_2)
$$

$$
Re[\frac{e^{-j\psi_1} + |\rho_R|}{1 + |\rho_R|e^{-j\psi_1}} \frac{e^{j\psi_2} + |\rho_R|}{1 + |\rho_R|e^{j\psi_2}}]
$$

$$
= \int \frac{d\psi_-}{2\pi} P(\psi_-) \tag{D.9}
$$

$$
Re[\int_0^{2\pi} \frac{\psi_2}{2\pi} \frac{e^{-j(\psi_- + \psi_2)} + |\rho_R|}{1 + |\rho_R|e^{-j(\psi_- + \psi_2)}}
$$

$$
\frac{e^{j\psi_2} + |\rho_R|}{1 + |\rho_R|e^{j\psi_2}}].
$$

The inner integral can be calculated by introducing a complex variable $z = e^{j\psi_2}$ in terms of which the inner integral becomes

$$
\frac{1}{2\pi j} \oint_{unitcircle} \frac{dz f(z)}{z(z + |\rho_R|e^{-j\psi_-})}, \tag{D.10}
$$

where $f(z) = (|\rho_R|z + e^{-j\psi_-})(z + |\rho_R|)/(1 + z|\rho_R|)$. Evaluating this integral via the residues at the two poles within the unit circle, $z = 0$ and $z = -|\rho_R|e^{-j\psi_-}$, we obtain

$$
\langle\cos(\phi_1 - \phi_2)\rangle = \int_0^{2\pi} \frac{d\psi_-}{2\pi} P(\psi_-)
$$

$$
[1 - \frac{(1 - |\rho_R|^4)(1 - \cos\psi_-)}{1 + |\rho_R|^4 - 2|\rho_R|^2\cos\psi_-}]. \tag{D.11}
$$

For the TRS case, $P_{\psi_-}(\psi_-) = \pi|\sin(\psi_-/2)|/2$, and Eq. (D.11) yields

$$
\langle\cos(\phi_1 - \phi_2)\rangle = \frac{|\rho_R|^4 + 2|\rho_R|^2 - 1}{2|\rho_R|^2}
$$

$$
+ \frac{(1 - |\rho_R|^2)^3}{4|\rho_R|^3} \ln\frac{1 + |\rho_R|}{1 - |\rho_R|}. \tag{D.12}
$$

For the TRSB case, $P_{\psi_-}(\psi_-) = 2\sin^2(\psi_-/2) = (1 - \cos\psi_-)$, and (D.11) yields

$$
\langle\cos(\phi_1 - \phi_2)\rangle = 1 - \frac{(|\rho_R|^2 - 1)(|\rho_R|^2 - 3)}{2}. \tag{D.13}
$$

BIBLIOGRAPHY

[1] T. H. Lehman and E. K. Miller, *Conference Proceedings: Progress in Electromagnetics Research Symposium*, Cambridge, MA, July 1–5, 1991, p. 428.

[2] J. G. Kostas and B. Boverie, IEEE Trans. EMC **33**, 366(1991).

[3] R. Holland and R. St. John, *Conference Proceedings: 10th Annual Review of Progress in Applied Computational Electromagnetics*, Monterey, CA, March, 1994, vol. 2, p. 554–568.

[4] R. Holland and R. St. John, *Statistical Electromagnetics* (Taylor and Francis, 1999), and references therein.

[5] R. H. Price, H. T. Davis, and E. P. Wenaas, Phys. Rev. E **48**, 4716 (1993).

[6] D. A. Hill, IEEE Trans. EMC **36**, 294 (1994); **40**, 209 (1998).

[7] L. Cappetta, M. Feo, V. Fiumara, V. Pierro and I. M. Pinto, IEEE Trans. EMC **40**, 185 (1998).

[8] E. P. Wigner, Ann. Math. **53**, 36 (1951); **62**, 548 (1955); **65**, 203 (1957); **67**, 325 (1958).

[9] F. Haake, *Quantum Signatures of Chaos* (Springer-Verlag, 1991).

[10] H. -J. Stöckmann, *Quantum Chaos* (Cambridge University Press, Cambridge, England, 1999).

[11] R. G. Newton, *Scattering theory of waves and particles* (McGraw-Hill, New York, 1966).

[12] V. Pagneux and A. Maurel, Phys. Rev. Lett. **86**, 1199 (2001).

[13] E. Doron, U. Smilansky and A. Frenkel, Phys. Rev. Lett. **65**, 3072(1990).

[14] P. W. Brouwer and C. W. J. Beenakker, Phys. Rev. B. **55** 4695 (1997).

[15] U. Kuhl, M. Martínez-Mares, R. A. Méndez-Sánchez and H. -J. Stöckmann, Phys. Rev. Lett., **94** 144101 (2005).

[16] S. Hemmady, X. Zheng, E. Ott, T. M. Antonsen and S. M. Anlage, Phys. Rev. Lett. **94**, 014102 (2005).

[17] Y. Alhassid, Rev. Mod. Phys. **72**, 895 (2000); C. W. J. Beenakker, Rev. Mod. Phys. **69**, 731 (1997).

[18] B. L. Altshuler et.al. *Mesoscopic phenomena in solids*, (North-Holland, Armsterdam, 1991).

[19] E. Ott, *Chaos in Dynamical Systems*, second edition (Cambridge University Press, 2002).

[20] M. C. Gutzwiller, *Chaos in Classical and Quantum Mechanics* (Springer-Verlag, 1990).

[21] P. A. Mello, Narendra Kumar, *Quantum Transport in Mesoscopic Systems* (Oxford University Press, New York, 2004).

[22] M. L. Mehta, *Random Matrices*, second edition (Academic Press, 1991).

[23] H. Weyl, Math. Ann. **77**, 313 (1916).

[24] R. B. Balian and C. Bloch, Ann. Phys. (N.Y.) **60**, 401 (1970); **63**, 592 (1971); **64**, 271 (1971).

[25] R. E. Prange, E. Ott, T. M. Antonsen, B. Georgeot and R. Blumel, Phys. Rev. E **53**, 207 (1996).

[26] M. C. Gutzwiller, J. Math. Phys. **8**, 1979 (1967); **10**, 1004 (1969).

[27] P. So, S. M. Anlage, E. Ott and R. N. Oerter, Phys. Rev. Lett. **74**, 2662 (1995).

[28] A. D. Mirlin, Phys. Rep. **326**, 260 (2000).

[29] S. W. McDonald and A. N. Kaufman, Phys. Rev. Lett. **42**, 1182 (1979); Phys. Rev. A **37**, 3067 (1988).

[30] O. Bohigas, M. J. Giannoni and C. Schmidt, Phys. Rev. Lett. **52**, 1 (1984).

[31] G. D. Birkhoff, Mathematica **50**, 359 (1927).

[32] H. -J. Stockmann and J. Stein, Phys. Rev. Let. **64**, 2215 (1990).

[33] S. Sridar, Phys. Rev. Lett. **67**, 785 (1991).

[34] E. Ott, Phys. Fluids **22**, 2246 (1979).

[35] M. V. Berry in *Chaotic Behavior of Deterministic Systems. Les Houches Summer School 1981* (North-Holland, 1983).

[36] S. -H. Chung, A. Gokirmak, D. -H. Wu, J. S. A. Bridgewater, E. Ott, T. M. Antonsen and S. M. Anlage, Phys. Rev. Lett. **85**, 2482 (2000).

[37] E. J. Heller, Phys. Rev. Lett. **53**, 1515 (1984).

[38] E. Bogomolny, Physica D **31**, 169 (1988).

[39] M. V. Berry, Proc. Roy. Soc. London Ser. A **423**, 219 (1989).

[40] T. M. Antonsen, E. Ott, Q. Chen, and R. N. Oerter, Phys. Rev. E **51**, 111 (1995).

[41] E. P. Wigner and L. Eisenbud, Phys. Rev. **72**, 29 (1947).

[42] A. M. Lane and R. G. Thomas, Rev. Mod. Phys. **30**, 257 (1958).

[43] C. Mahaux and H. A. Weidenmuller, *Shell-Model Approach to Nuclear Reactions* (North-Holland, Amsterdam, 1969).

[44] J. J. M. Verbaarschot, H. A. Weidenmüller and M. R. Zirnbauer Phys. Rep. **129**, 367 (1985).

[45] C. H. Lewenkopf and H. A. Weidemüller, Ann. of Phys. **212** 53, (1991).

[46] Y. V. Fyodorov and H. J. Sommers, J. Math. Phys. **38**, 1918 (1997).

[47] R. A. Jalabert, A. D. Stone and Y. Alhassid, Phys. Rev. Lett. **68**, 3468 (1992).

[48] M. V. Berry J. Phys. A. **10** 2083 (1977).

[49] P. W. Brouwer, Phys. Rev. B **51**, 16878 (1995).

[50] T. J. Krieger, Ann. of Phys. **42**, 375(1967).

[51] P. A. Mello, in *Mesoscopic Quantum Physics* edited by E. Akkermans, G. Montambaux, J. L. Pichard and J. Zinn-Justin (North Holland, Amsterdam, 1995).

[52] http://www.ansoft.com/products/hf/hfss/.

[53] F. J. Dyson, J. Math. Phys. **3**, 140 (1962)

[54] X. Zheng, T. M. Antonsen and E. Ott accepted by *Electromagnetics*, preprint cond-mat/0408327.

[55] X. Zheng, T. M. Antonsen and E. Ott accepted by *Electromagnetics*, preprint cond-mat/0408317

[56] Y. Alhassid, and C. H. Lewenkopf, Phys. Rev. Lett. **75** 3922 (1995).

[57] L. K. Warne, K. S. H. Lee, H. G. Hudson, W. A. Johnson, R. E. Jorgenson and S. L. Stronach, IEEE Trans. on Anten. and Prop. **51** 978 (2003).

[58] P. A. Mello, P. Peveyra, and T. H. Seligman, Ann. of Phys. **161**, 254 (1985); G. López, P. A. Mello and T. H. Seligman, Z. Phys. A, **302**, 351 (1981).

[59] D. V. Savin, Y. V. Fyodorov and H. -J. Sommers, Phys. Rev. E. **63**, 035202 (2001).

[60] R. A. Méndez-Sánchez, U. Kuhl, M. Barth, C. H. Lewenkopf and H. -J Stöckmann, Phys. Rev. Lett. **91**, 174102 (2003).

[61] U. Kuhl, M. Martínez-Mares, R. A. Méndez-Sánchez and H. -J. Stöckmann, Phys. Rev. Lett., **94** 144101 (2005).

[62] H. Alt, H. -D. Gräf, H. L. Harney, R. Hofferbert, H. Lengeler, A. Richter, P. Schardt, and H. A. Weidenmüller, Phys. Rev. Lett. **74**, 62 (1995).

[63] E. Kogan, P. A. Mello and H. Liqun, Phys. Rev. E. **61**, R17 (2000).

[64] S. Hemmady, X. Zheng, T. M. Antonsen, E. Ott, and S. M. Anlage, Phys. Rev. E **71**, 056215 (2005).

[65] K. B. Efetov and V. N. Prigodin, Phys. Rev. Lett. **70**, 1315 (1993); A. D. Mirlin and Y. V. Fyodorov, Europhys. Lett. **25**, 669 (1994).

[66] N. Taniguchi, V. N. Prigodin, Phys. Rev. B. **54**, 14305 (1996).

[67] Y. V. Fyodorov and D. V. Savin, JETP Lett., **80**, 725 (2004); D. V. Savin and H. -J. Sommers, Phys. Rev. E **69** 035201 (2004).

[68] C. W. J. Beenakker and P. W. Brouwer, Physica E. **9**, 463 (2001).

[69] V. Gopar, P. Mello, and M. Büttiker, Phys. Rev. Lett. **77**, 3005(1996).

[70] J. F. Cornwell, *Group Theory in Physics: an Introduction* (Academic Press, San Diego, California, 1997).

[71] P. A. Lee and T. V. Ramakrishnan, Rev. Mod. Phys. **57**, 287 (1985); G. Bergmann, Phys. Rep. **107**, 1 (1984).

[72] C. Fiachetti and B. Michielsen, Elect. Lett. **39**, 1713 (2003).

[73] W. Hauser and H. Feshbach, Phys. Rev. **87**, 366 1952.

[74] W. A. Friedman and P. A. Mello, Ann. of Physics, **161**, 276 (1985).

[75] D. Agassi, H. A. Weidemüller, and G. Mantzouranis, Phys.Rep. **22** 145 (1975).

[76] D. V. Savin, Y. V. Fyodorov and H. -J. Sommers, Proceedings of 2nd Workshop on "Quantum Chaos and Localization Phenomena", May 19-22, 2005, Warsaw.

[77] X. Zheng, S. Hemmady, T. M. Antonsen, S. M. Anlage, and E. Ott, submit to Phys. Rev. E., preprint: cond-mat/0504196.

[78] A. Gokirmak, D. -H. Wu, J. S. A. Bridgewater and S. M. Anlage, Rev. Sci. Instrum. **69**, 3410 (1998).

[79] P. So, S. M. Anlage, E. Ott and R. N. Oerter, Phys. Rev. Lett. **74**, 2662 (1994).